(2)

Semi-Annual Report

Growth, Nitrogen Vacancy Reduction and Solid Solution Formation in Cubic GaN Thin Films and the Subsequent Fabrication of Superlattice Structures Using AlN and InN

Supported under Grant #N00014-86-K-0686 P5
Innovative Science and Technology Office
of the Strategic Defense Initiative
Office of the Chief of Naval Research
Report for the period January 1, 1990–June 30, 1990

Robert F. Davis, Michael J. Paisley and Zlatko Sitar
Materials Science and Engineering Department
North Carolina State University
Campus Box 7907
Raleigh, NC 27695-7907

July, 1990

REPORT DOCUMENTATION PAGE

Form Approved
OMB No 0704-0188

1. AGENCY USE ONLY (Leave blank)	2. REPORT DATE	3. REPORT TYPE AND DATES COVERED
	July, 1990	Semi-Annual 1/1/90-6/30/90

4. TITLE AND SUBTITLE Growth, Nitrogen Vacancy Reduction and Solid Solution Formation in Cubic GaN Thin Films and the Subsequent Fabrication of Superlattice Structures Using AlN and InN

5. FUNDING NUMBERS
R&T:s400001srq05
S.O.:1114SS

6. AUTHOR(S)
Robert F. Davis

7. PERFORMING ORGANIZATION NAME(S) AND ADDRESS(ES)
North Carolina State University
Hillsborough Street
Raleigh,NC 27695

8. PERFORMING ORGANIZATION REPORT NUMBER
N00014-86-K-0686 P5

9. SPONSORING/MONITORING AGENCY NAME(S) AND ADDRESS(ES)
Sponsoring: ONR, 800 N. Quincy, Arlington, VA 22217
Monitoring: Office of Naval Research Resider, N66005
The Ohio State Univ. Research Center
1314 Kinnear Road
Columbus, OH 43212-1194

10. SPONSORING/MONITORING AGENCY REPORT NUMBER

11. SUPPLEMENTARY NOTES

12a. DISTRIBUTION/AVAILABILITY STATEMENT
Approved for Public Release; Distribution Unlimited

12b. DISTRIBUTION CODE

13. ABSTRACT (Maximum 200 words)

In the research of this reporting period, AlN films and AlN/GaN layered structures have been grown and structurally, chemically and optically characterized. In addition, BN has been similarly deposited on cubic (β)-SiC and diamond substrates. Strained layer superlattices have been fabricated for the first time between GaN and AlN. The energy offset was up to 260 meV for the superlattices with the thinnest barriers. Cubic BN was deposited on the aforementioned substrates; however, significant carbon was also present. The latter problem has now been resolved.

14. SUBJECT TERMS	15. NUMBER OF PAGES
aluminum nitride, boron nitride, layered structures, transmission electron microscopy, photoluminescence, electron cyclotron resonance plasma source, (JES)	69
	16. PRICE CODE

17. SECURITY CLASSIFICATION OF REPORT	18. SECURITY CLASSIFICATION OF THIS PAGE	19. SECURITY CLASSIFICATION OF ABSTRACT	20. LIMITATION OF ABSTRACT
UNCLAS	UNCLAS	UNCLAS	SAR

NSN 7540-01-280-5500

Standard Form 298 (Rev. 2-89)
Prescribed by ANSI Std. Z39-18
298-102

Table of Contents

I. Introduction 1

II. Aluminum Nitride and AlN/GaN Layered Structures 4

A. Growth Procedure 4
B. Chemical Analysis 5
C. Structural and Microstructural Analyses 6
X-ray Rocking Curves 6
Transmission Electron Microscopy 12
D. Optical Characterization 16

III. Boron Nitride 23

A. Boron Nitride on Silicon Carbide 23
Overview 23
Chemical Analysis 23
Structural Analysis 27
B. Boron Nitride on Diamond (100) 29
C. Laser Ablation 33
D. Characterization of Sumitomo c-BN 36
E. Future Research 38
Gas Source MBE 38
Laser Ablation 40
Analytical Techniques 42

IV. References 42

Appendix: Electron Cyclotron Resonance (ECR) Plasma Source

A-I. Introduction 45

A-II. Description of the NCSU-ECR Plasma Source 46

Source head 46
Magnets 48
Microwave system 50

A-III. Plasma Characteristics 51

A-IV. Growth Results 58

A. Gallium Nitride Layers 58
Overview 58
Structural Analysis 59
B. Mg-Doping of GaN 64

A-V. References 65

I. Introduction

Solid state electronic devices for sources and detectors of light have made possible products ranging from simple light emitting diodes to more complex systems, such as the compact disk player and optical mass storage media for computers.

Recent advances in tailoring the physical properties of bulk semiconductors have been matched by deposition technologies that allow the growth of monocrystalline thin films with film thickness controlled to atomic dimensions. The techniques—molecular-beam epitaxy, atomic layer epitaxy and metal-organic chemical vapor deposition—require ultraclean conditions and depend on layer-by-layer growth of material to achieve epitaxy. Such epitaxial film structures, especially those made from microstructural combinations of GaAs and GaAlAs, have been used to make several important electronic and optoelectronic devices. However, one limitation of the $Ga_xAl_{1-x}As$ system in terms of optoelectronic materials is that the relatively small bandgaps of GaAs (1.35 eV) and AlAs (2.16 eV) restrict optical sources based on these materials to the red and near infrared regions of the spectrum. Because of that limitation, materials having larger bandgaps are now being investigated. One group of materials having both wider bandgaps and direct transitions between the conduction and valence bands is the III-V nitrides, specifically AlN, GaN and InN.

Gallium nitride (GaN) is a III-V compound semiconductor having a direct, wide bandgap (3.5 eV at 300K) as well as a large saturated electron drift velocity. This unique combination of properties coupled with appropriate doping provides the potential for fabrication of short wavelength semiconductor lasers, LEDs and detectors as well as transit-time-limited (IMPATT, etc.) microwave power amplifiers from this material. In addition, aluminum nitride (AlN) and indium nitride (InN), are direct bandgap materials of 1.95 eV and 6.28 eV, respectively. These other nitrides form a solid solution series with GaN, which will permit bandgap and lattice parameter engineering in order to fabricate the devices noted above.

Bandgap engineering in the range of 3.4–6.2 eV can be achieved either by solid solutions or by layered structures of GaN and AlN. So far only AlGaN solid solutions have been studied.[1-3] The superlattices are favored for several reasons. As has been shown for the GaAs/GaAlAs system,[4-7] optoelectronic devices using multi–quantum well structures instead of solid solutions exhibit lower threshold current density, lower non–radiative recombination rate, narrower emission spectra and reduced sensitivity to temperature. The lattice parameter mismatch between AlN and GaN is only 3.5%, thus layered structures of these two materials offer a way of producing high quality, low dislocation density GaN- and/or AlN-based materials and devices. To our knowledge, layered structures of these two materials have not been produced prior to this investigation.

The current research has achieved this objective via the use of molecular beam epitaxy (MBE) and the related technique of atomic layer epitaxy (ALE), substrate temperatures ≤700°C, and atomic nitrogen sources. The present growth method involves the deposition of gallium (and/or aluminum or indium) from a standard effusion cell and atomic nitrogen from a remote microwave electron cyclotron resonance (ECR) plasma source (designed and commissioned at NCSU) onto various substrates (whose temperature is considerably lower than that required for CVD). It has been demonstrated that the higher reactivity of the nitrogen atoms will result in a more complete incorporation of nitrogen into the GaN and AlN films with the corresponding increase in growth rate and reduction of excess nitrogen vacancies.

The remaining nitride in Group IV is that of boron nitride (BN). Boron nitride has long been known for its desirable properties as a highly insulating as well as a chemically and thermally stable material. It is structurally similar to carbon in that it exists in hexagonal, wurtzitic, and cubic forms. The cubic form has received much interest recently as a possible substrate for the deposition of diamonds, as a deposited electronically active film on diamond due to the similar lattice parameters

(Δa_o=1.34%) and its wider bandgap.[16] Thus the fabrication of a cBN/diamond heterostructure wherein electrons can be injected from the cBN into a pure diamond substrate would allow one to take advantage of the high electron mobility of the diamond.

In terms of optoelectronics, it is cBN that is desired. Unlike the other nitrides, it is an indirect bandgap material; however, it can be doped with both n- and p-type materials. Thus ultraviolet high emitting diodes are possible and have been produced. Moreover, if the bandgap is determined to be ≥6.6 eV, it will be useful as a solar blind detector and window.

Several approaches have been employed, in the attempt to grow thin films of cubic boron nitride (c-BN). These include reactive diode and rf sputtering, ion implantation, plasma CVD, and ion beam techniques. All these attempts were successful in producing polycrystalline films of c-BN, though predominantly of a mixed nature with both cubic and other phases present. It appears that most researchers succeeded in the deposition of c-BN if the technique included the input of additional energy from energetic ions during the deposition process. In the present study, growth of cubic boron nitride (zincblende structure) films has been attempted on a variety of substrates and under widely varying conditions which are described in detail in Section III.

In the research of this period, AlN films and AlN/GaN layered structures have been grown and structurally, chemically and optically characterized. In addition, BN has been similarly deposited on cubic SiC and diamond substrates. The procedures, results and conclusions of this research are described in the following sections. Finally, a recently submitted paper concerned with the design, fabrication, operation and employment of the NCSU-designed ECR source is given in an appendix.

II. Aluminum Nitride and AlN/GaN Layered Structures

A. Growth Procedure

Growth studies were conducted on (0001)-oriented α-SiC (6H polytype) and (0001) oriented epitaxial quality sapphire substrate wafers, both of which have a hexagonal structure. All substrates were cleaned to remove organic and metallic contaminants using the following sequence of chemicals, temperatures and times: 1:1:5 solution of HNO_3:H_2O_2:H_2O at 75°C for 5 min, DI water rinse for 1 min, 1:1:5 solution of HCl:H_2O_2:H_2O at 75°C for 5 min and DI water for 5 min. The α-SiC wafers were subsequently oxidized in flowing dry oxygen at 1200°C for 1.5 hrs in order to consume an ≈50 nm thick surface layer of the wafer which contained polishing damage. To remove this oxide layer the substrates were etched for 1 min in 49% HF and rinsed in DI water prior to loading into the MBE system. These last two chemical procedures were also performed on the sapphire wafers. All substrates were then mounted on a standard 3 inch molybdenum block with indium which provided both good adherence and thermal contact.

The substrates underwent an initial low temperature (≈70°C) outgasing in the load lock followed by slow heating in the transfer tube to a maximum of 900°C with a dwell time of 30 min at this temperature. After cooling, the samples were introduced into the growth chamber and examined by reflection high energy electron diffraction (RHEED) using a 10 kV beam. The resulting RHEED patterns on both the α-SiC and sapphire substrates showed Kikuchi lines indicative of good crystalline quality.

Prior to growth, the substrates were heated to the desired deposition temperature and subsequently exposed to a flux of plasma activated nitrogen species for about 5 min. No change in the RHEED pattern occurred as a result of this procedure. Following the stabilization of temperatures and fluxes, a 140 nm thick GaN buffer layer was grown followed by 20 to 200 periods of AlN/GaN layers having the

thickness for a given deposition in the range of 1.5–40 nm. The growth conditions are summarized in Table I.

Table I. Growth Conditions

Nitrogen pressure	$1x10^{-4}$ Torr
Microwave power	50 W
Gallium temperature	990°C
Aluminum temperature	1120°C
Substrate temperature	400–750°C
Growth rate:	
GaN	≈2.5 nm/min
AlN	≈1.6 nm/min
GaN buffer layer thickness	140 nm
Period thickness	1.5–40 nm
Number of periods	20–200
Total growth time	6–7 hrs

After the total growth sequence was completed, the gallium and aluminum cells and the substrate were cooled, while the nitrogen source remained active. This source was turned off and the growth chamber returned to UHV conditions once the substrate temperature was below 400°C. The sample was again evaluated with RHEED to determine the crystal structure and to obtain an initial estimate of the film quality.

B. Chemical Analysis

Scanning Auger microprobe (SAM) (JEOL JAMP-30) analysis was used to determine the presence of impurities and the nominal compositions of the AlN and GaN layers. Auger spectra taken from the untreated surface showed oxygen and carbon surface contamination due to exposure of the film to the atmosphere. Figure 1 shows an Auger depth profile taken from a sample with 20 AlN/GaN double layers. The layers of each material were 10 nm thick. The profile indicates well defined layers. The samples with thicker layers also showed well defined and sharp interfaces. The

quality of the interfaces could not be confirmed by SAM in the case of very thin multilayers, since the escape depth for Auger electrons is about 4–5 nm and because the depth resolution of the sputtering process, which roughens the surface, is in the same range. The Auger spectra presented in Figure 2 were taken from the fourth AlN and the fifth GaN layers of the sample noted in Figure 1. The spectra indicate nominal AlN and GaN compositions and some mixing of Ga and Al in AlN and GaN layers, respectively. A small amount of interfacial mixing may be present; however, TEM observations (see below) revealed well defined layers and thus indicate that the Auger data exaggerate this phenomenon for the reasons stated above. There is also a trace of oxygen contamination which decreased with the distance from the surface. As such, the oxygen peak may, at least partially, be due to the transfer of surface contaminants to the exposed material by ion beam sputtering. No other contaminants were observed within the resolution of the instrument (typically ≈ 0.1 at. %).

C. Structural and Microstructural Analyses

X-ray Rocking Curves. The AlN/GaN layered structures were subsequently analyzed by x–ray diffractometry. The $CuK\beta$ line was used instead of filtered $CuK\alpha$ one to obtain a truly monochromatic x–ray line and, therefore, unambiguous determination of the AlN/GaN period and the crystalline quality of the superlattices produced in each deposition. The spectra were obtained around the expected (0002) reflections for "bulk" AlN and GaN.

A perusal of Figure 3 reveals that the diffraction spectra of the layered structures are much more complex than those for bulk crystals and single thin films. This is to be expected, since the lattice parameters in the direction normal to the layers (in our case (0001)) are different for AlN and GaN. Moreover the lattice parameters perpendicular to the surface depend upon the distortion of the lattice caused by the interlayer strain, and, as such, the diffraction peaks appear at different

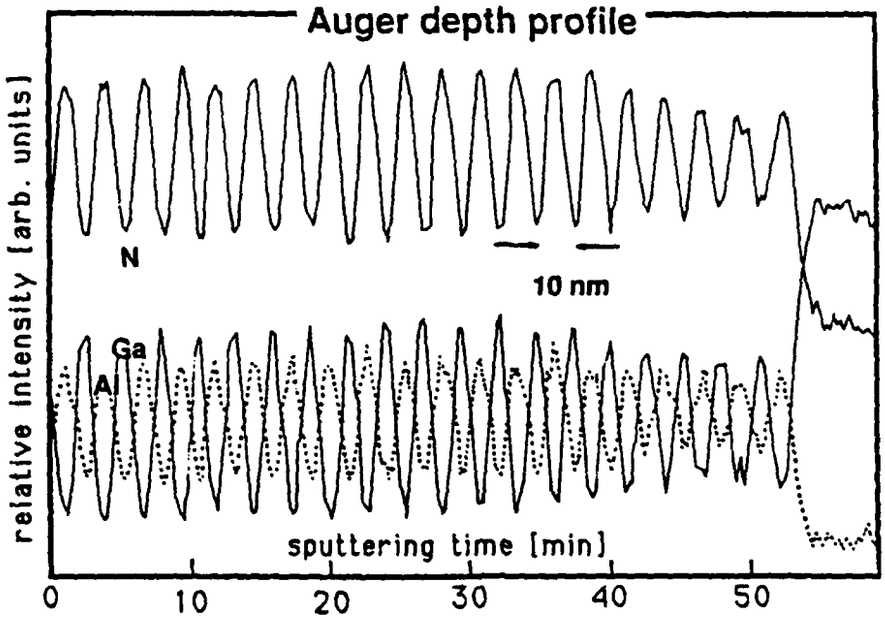

Figure 1. Auger depth profile taken from a sample with 20 AlN/GaN double layers. The layers of each material were 10 nm thick.

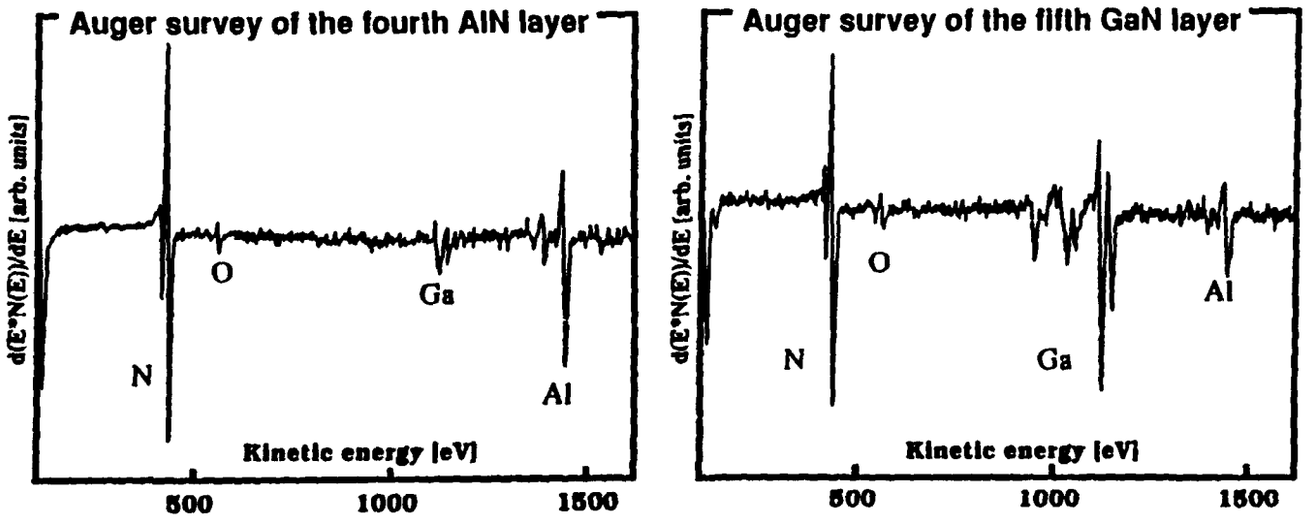

Figure 2. Auger spectra taken from the fourth AlN and fifth GaN layers of the sample noted in Figure 4. The apparent mixing of Al in GaN and Ga in AlN is probably an artifact (see text). Spectra indicate a trace of oxygen contamination.

positions than one would expect from the bulk properties of the materials. The layered structure also introduces additional periodicity in the growth direction which is revealed in the diffraction spectra as well. Finally, the diffraction spectra usually contain a peak from the substrate or the buffer layer which is often much stronger than the superlattice peaks. These superimposed peaks are convenient for the determination of the strain in the layers[11,12] but make diffraction spectra even more complicated and difficult to read.

Figures 3(a1–a6) show the evolution of the diffraction peaks as a function of decreasing AlN/GaN bilayer periodicity, P, which is given as

$$P = t_{AlN} + t_{GaN} \quad (1)$$

where t_{AlN} and t_{GaN} are the respective thicknesses of the individual layers of AlN and GaN. Each spectrum shows the (0002) diffraction peak from the GaN buffer layer and the zero order superlattice peak (marked "0"), which represents the average vertical lattice parameter of the superlattice, and associated satellite peaks (marked from -4 to 3). The buffer layer peak is superimposed on the latter peaks making the diffraction from the superlattice unclear. As such, each spectrum in Figure 3(a1-a6) was fitted with a sum of Lorentzian peaks followed by the subtraction of both the buffer layer peak and the overall background, which made the evolution of the peaks with the change of superlattice period easier to visualize. The resulting spectra are shown in Figure 3(b1–b6). In this latter set of spectra, the x–ray intensities are plotted as a function of 2/c, where c is the lattice parameter perpendicular to the surface. This is convenient for measuring parameters (P, t_{AlN}, t_{GaN}, c_{GaN}, c_{AlN}) directly from the spectra.

A representative diffraction spectrum having marked parameters characteristic of a superlattice produced in this study is shown in Figure 3(b1). Several parameters can be determined, as indicated, by measuring reciprocal distances on the spectrum. The periodicity of the superlattice, P, is inversely proportional to the angular spacing of

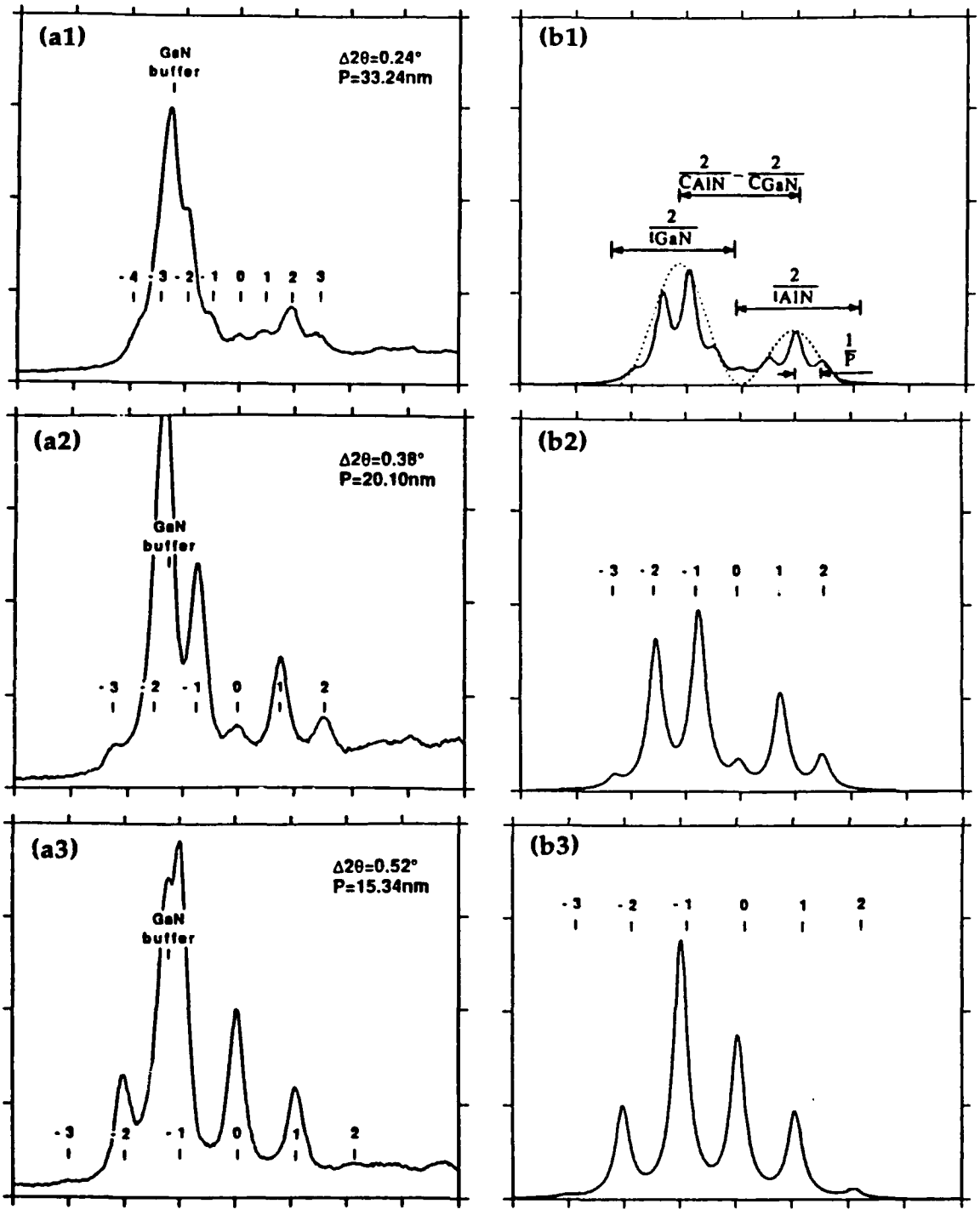

Figure 3. (a) X-ray diffraction spectra of the samples with different periodicities. Each pattern is characterized by the (0002) peak from the GaN buffer layer (marked by "GaN buffer") and a zero-order peak from AlN/GaN layers at 2q = 32° (marked by "0") with satellite peaks around it. An angular spacing, D2q, of satellite peaks and a calculated bilayer period, P, is given for each spectrum. (b) Diffraction spectra after the subtraction of the GaN buffer layer peak and the overall background. Figure (b1) illustrates the use of the spectra for the determination of different parameters (see text).

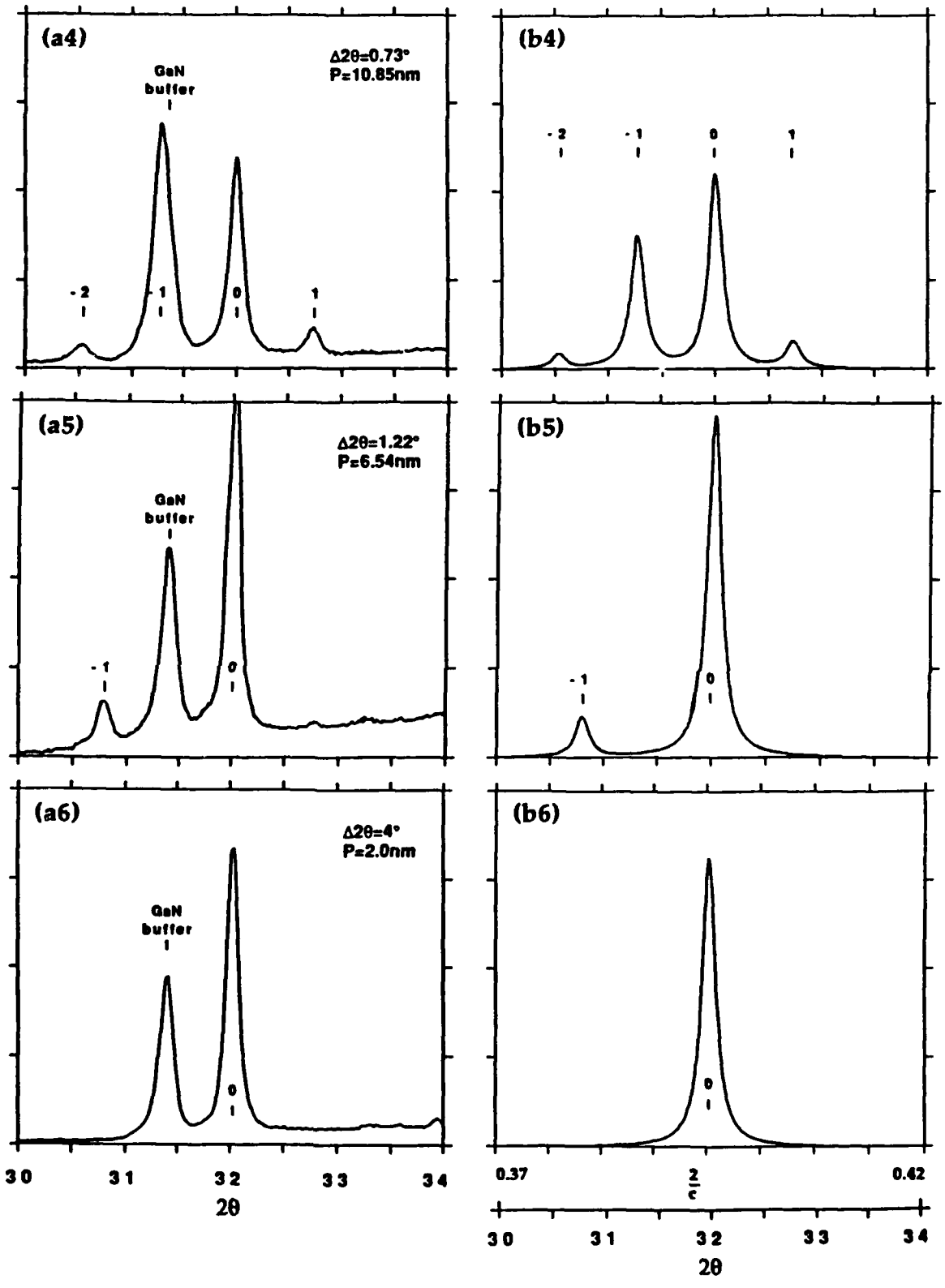

Figure 3. Continued

the satellite peaks. The values of t_{AlN} and t_{GaN} can be estimated from the widths of the envelopes (dotted curves) of the AlN and GaN sets of peaks. The perpendicular lattice parameters of the two materials in the individual layers are measured from the angular positions of the envelopes. Finally, the strain in the layered structure can be estimated by comparing the angular positions of the buffer layer peak with the superlattice peaks.

Figures 3(b1) and 3(b2) show two almost completely separated sets of superlattice peaks, each of which represents one of the two materials. Since the envelope widths of the two materials are proportional to $\frac{1}{t_{AlN}}$ or $\frac{1}{t_{GaN}}$ and their separation scales with $\frac{1}{c_{AlN}} - \frac{1}{c_{GaN}}$, we have the following condition for the two sets of peaks, taken around the (0002) pole, to be well separated:

$$\frac{2}{c_{AlN}} - \frac{2}{c_{GaN}} > \frac{1}{t_{AlN}} + \frac{1}{t_{GaN}}. \qquad (2)$$

For example, if we assume that the lattice parameter perpendicular to the surface for each material has the same value as the bulk (as will be seen later, this is a reasonable assumption for thick layers) and take t_{AlN} equal to t_{GaN}, both sets of peaks are well separated for P>28 nm, which is in good agreement with the measured spectra. In Figure 3(b3) both sets of peaks begin to overlap, and the positions of the two envelopes become less obvious. As one moves toward even shorter periods the two envelopes can no longer be resolved, as their widths become much larger than their spacing. As a consequence of these shorter periods the number of observable satellite peaks decreases. Figure 3(b6), which represents the diffraction spectrum of a superlattice with P=2 nm, shows only the zero–order superlattice peak which is located approximately midway between the expected peaks for pure AlN and pure GaN. The peak corresponds to an interplanar spacing of 0.252 nm, which is intermediate between the spacings of the (0002) planes of AlN (0.249 nm) and GaN

(0.258 nm) and represents the average spacing of the (0002) planes in the superlattice. Satellite peaks for this sample are out of the range of the scan, and are expected to be at ≈28° and ≈36°. As noted above, TEM results show a well defined layered structure; thus, there is no reason to believe that this peak arises from the homogeneous mixing of the two materials.

For superlattices with periodicities over 20 nm (see Figures 3(b1–b2)) the center of GaN envelope coincides with the GaN buffer layer peak. This indicates that both have the same vertical lattice spacings. Since the center of the AlN envelope also appears at the same angular position as one would expect for the (0002) peak of pure AlN, this indicates that individual layers at periods larger than 20 nm have unchanged vertical lattice parameters and thus are relaxed with respect to each other. At periods smaller than 20 nm the positions of the envelopes start changing (compare Figures 3(b2–b3)). This is believed to be related to the lattice distortion due to elastic strain. However, since the overlapping of both envelopes starts at about the same layer period, the quantitative displacements of the centers are not clear, and become even less evident at superlattices with periods smaller than 10 nm (see Figures 3(b4-b6)). In order to more accurately determine the transition between relaxed and strained structures, the reflections from the planes with mixed indices (for example $(10\bar{1}1)$) should be studied.

Transmission Electron Microscopy. Transmission electron microscopy (TEM) (Hitachi H-800) and high resolution microscopy (HREM) (JEOL 200CX) were used to further analyze the AlN/GaN layered structures. Cross-sectional TEM specimens were prepared using standard techniques[10].

The periodicities calculated from the x-ray spectra were confirmed by the TEM images. Discrepancies between the two methods were found to be less than 5%.

Superlattices grown on α–SiC showed a high degree of crystallinity, which has been confirmed by RHEED, X–ray diffraction, and transmission electron diffraction.

Figure 4 shows a TEM image of 5 nm thick layers of AlN and GaN. GaN layers are dark; those of AlN are light. Layers are well defined and have few structural defects. The $(10\bar{1}1)$ diffraction pattern (inset), taken from the layered structure, confirms the monocrystalline nature of the film with a low density of structural defects. The slight waviness of the layers appears to start at the buffer layer; it becomes more defined toward the top of the film. Similar phenomenon has been observed in GaAs/GaAlAs systems[13,14] and is induced due to the optimum growth temperature difference between the two materials. In the films with thicker AlN/GaN layers this effect is observed as interface roughness between the individual layers, rather than waviness of the layers. This can be seen in Figure 5 which shows 20 nm thick layers.

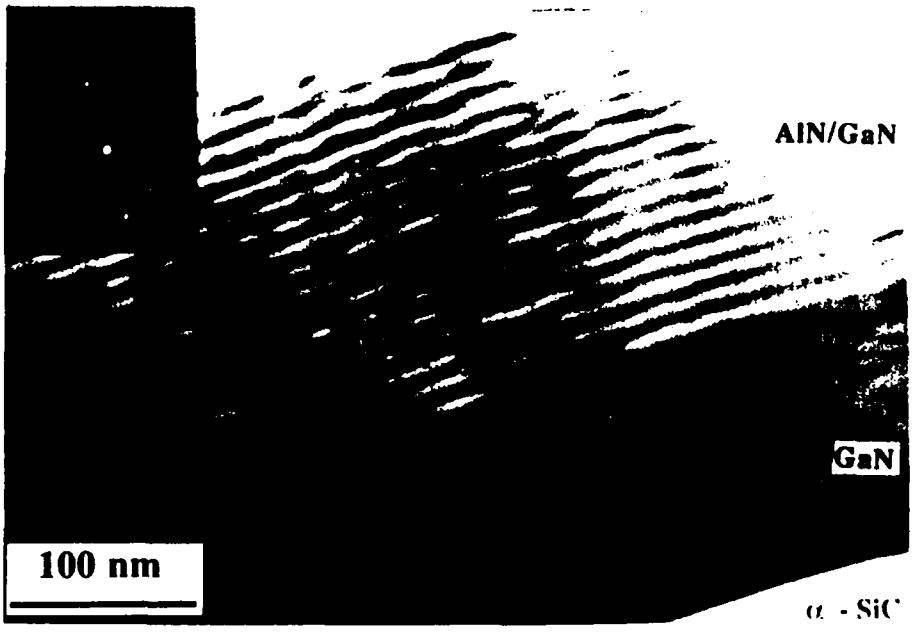

Figure 4. AlN/GaN layered structure grown on α(6H)-SiC. The thickness of the individual layers is 5 nm.

By contrast, structures grown on sapphire were oriented polycrystalline. These films showed a columnar structure. The range of misorientation of the individual crystallites, measured from the lattice fringes, was found to be from 0° to 8°. However,

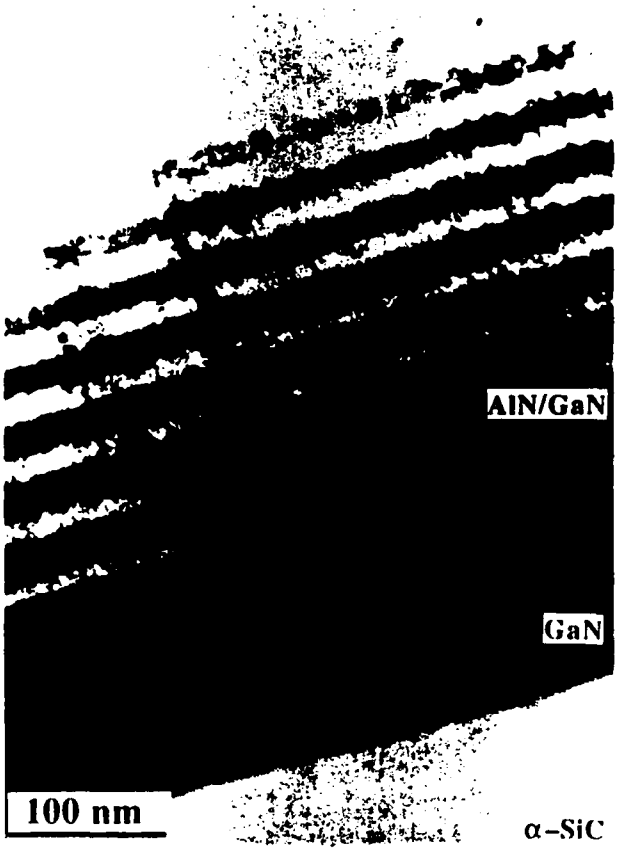

Figure 5. AlN/GaN layered structure grown on α(6H)-SiC. The thickness of the individual layers is 20 nm.

layers of the two materials within individual crystallites are well defined and no misfit dislocations or other defects have been found. The HREM image of 3 nm thick individual layers in Figure 6 indicates perfectly strained material, with uninterrupted lattice fringes at the transitions from one material to the other. Even the structure containing 0.5 nm thick AlN layers (2 monolayers) and 1 nm thick AlN layers (4 monolayers), shown in Figure 7, shows very good compositional contrast between the individual layers.

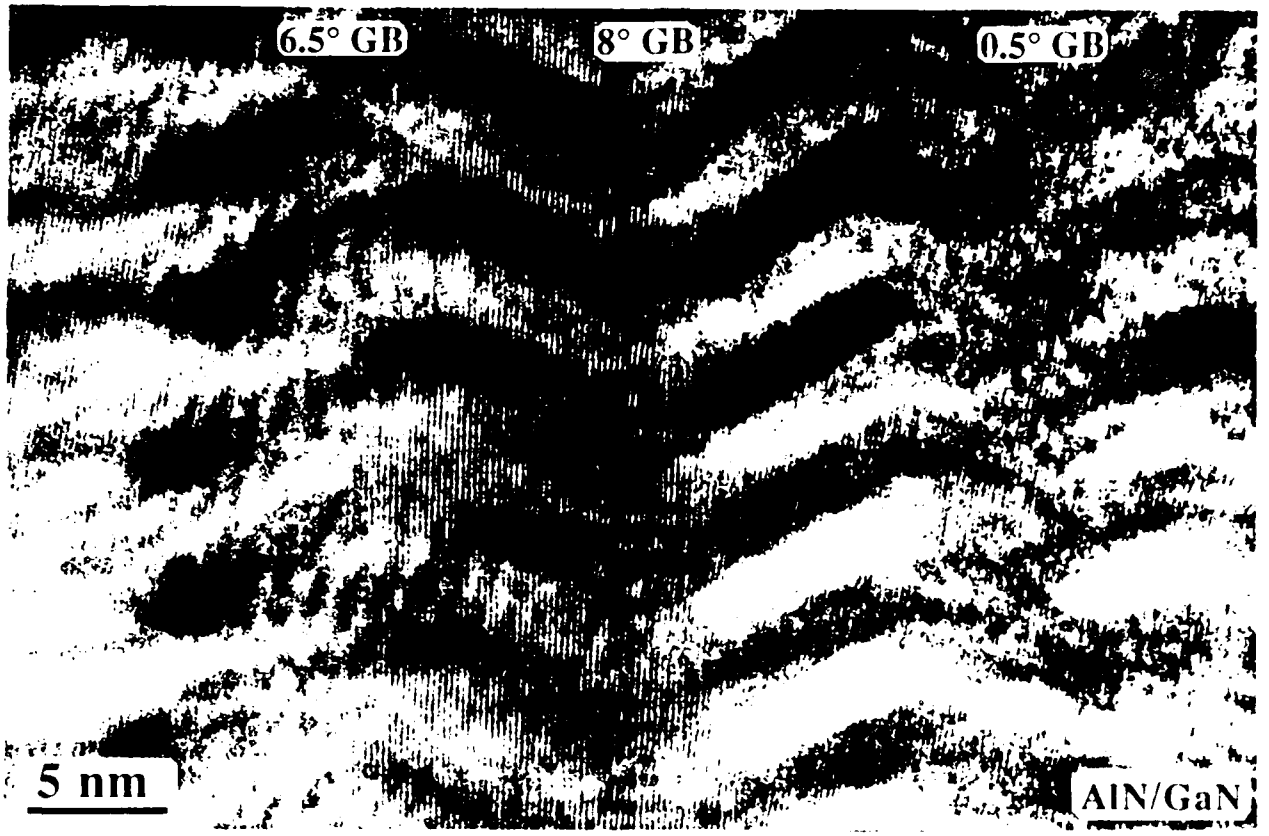

Figure 6: AlN/GaN layered structure grown on sapphire. The thickness of the individual layers is 3 nm. Note misorientation of the individual crystallites in the columnar structure.

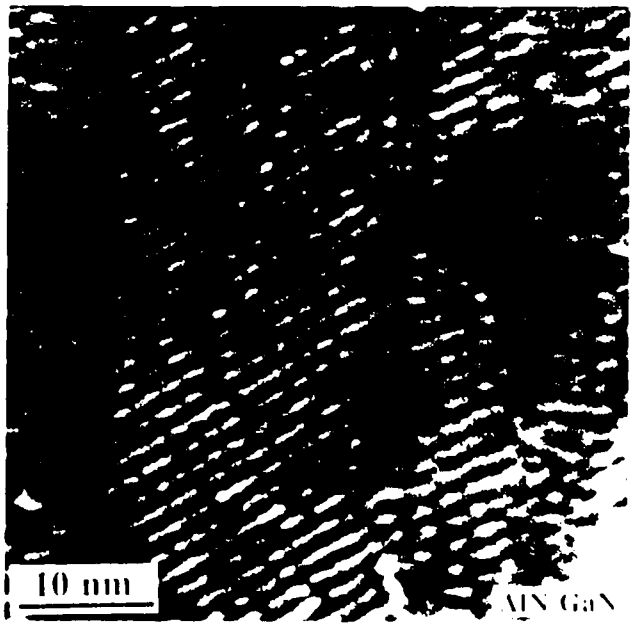

Figure 7: AlN/GaN layered structure grown on sapphire. The thickness of AlN and GaN layers is 0.5 nm and 1 nm, respectively.

D. Optical Characterization

The samples grown on α(6H)-SiC were characterized optically by cathodoluminescence. The spectra were taken at 77 K in the wavelength range of 200 to 800 nm using the excitation electron beam energies of 7 keV.

The bandgap difference between AlN and GaN is almost 3 eV. Thus layers of these two materials produce almost one order of magnitude larger band discontinuities than are achieved in AlGaAs or InGaAs systems. As such, AlN/GaN superlattices may provide some interesting insights regarding the behavior of electrons and holes. For example, they have potential of providing several well–separated confined electronic states.

Spectra taken from the samples with AlN/GaN layer thicknesses of 1/1, 0.5/1, 3/3, and 10 nm/10 nm (0.25 nm ≈ one monolayer) are shown in Figure 8. Each spectrum consists of a broad structure centered around ≈500 nm (2.5 eV), and a well defined peak at a higher energy. The former is due to the luminescence from the α(6H)-SiC substrate.

The higher energy peak increases in energy as the thickness of the layers in different samples decreases. The peak position moves from 3.42 eV for the sample with 10 nm thick wells and barriers, to 4.11 eV for the sample with 1 nm layers. The emission energy from a multi-quantum well structure is expected to also decrease if the well thickness remains constant and the barrier thickness decreases. This effect, which is due to an increase in tunneling probability through thinner barriers, is demonstrated in peaks 1/1 and 0.5/1 which are from structures with 1 nm thick GaN wells and 1 nm and 0.5 nm thick AlN barriers, respectively.

Peaks at higher energies are also expected for AlGaN solid solutions. For example, the emission at 4.1 eV is expected for a molar concentration of Al of 0.32.[3] According to the structural and chemical analyses, there is no reason to believe that a homogeneous solid solution close to this composition had formed. Moreover, random

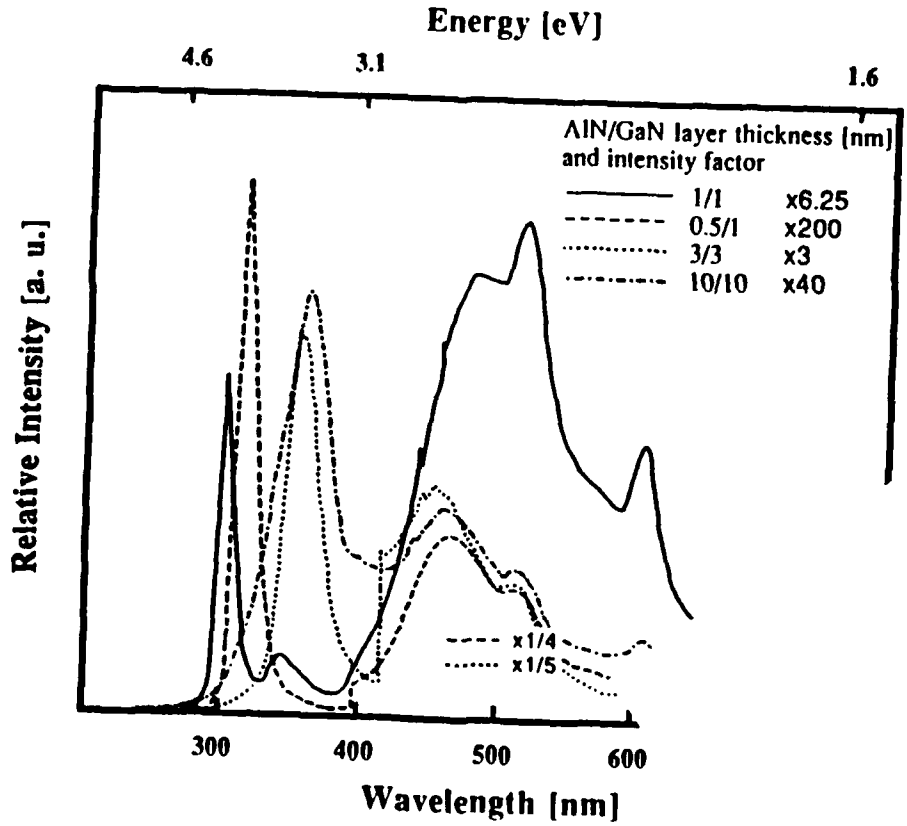

Figure 8: Cathodoluminescent spectra taken at 77K of the AlN/GaN layered structures with different periodicities. Broad peak above 400 nm is due to SiC substrate. High energy peaks are from AlN/GaN layers. Emission energy decreases with increasing GaN well thickness (1/1, 3/3, 10/10) and decreasing AlN barrier thickness (1/1, 0.5/1)

mixing, which may be to some extent present at rough interfaces, would not result in strong, well defined peaks. On this basis, we interpret the high energy peak to be due to the recombination of the electrons and holes confined in the GaN wells. As such, we believe, that the spectra demonstrate the formation of the quantized electronic states.

A computer model for the for the calculation of the band structure of AlN/GaN superlattices has been developed and a comparison between the theory and experiments has been made. Two different cases were examined: 1) The emission energy shift as a function of the layer thickness, while the thicknesses of GaN and

AlN layers were maintained equal (i. e. $t_{AlN} = t_{GaN} = \frac{P}{2}$), and 2) emission energy shift as a function of the barrier thickness (AlN), while the well thickness (GaN) was maintained constant at 1 nm.

The allowed energy bands for the electrons in the conduction band and for the holes in the valence band in the superlattice were calculated using a one-dimensional Krönig–Penney model.[15] According to this an electron or a hole can occupy a particular energy state in the superlattice only, if the following is true:

$$\left|\cos\left[\frac{t_1(2mE)^{\frac{1}{2}}}{\hbar}\right]\cosh\left[\frac{t_2(2m(V-E))^{\frac{1}{2}}}{\hbar}\right] + \right.$$

$$\left. + \left(\frac{V}{E}-1\right)^{\frac{1}{2}}\left(\frac{V}{2E}-1\right)\sin\left[\frac{t_1(2mE)^{\frac{1}{2}}}{\hbar}\right]\sinh\left[\frac{t_2(2m(V-E))^{\frac{1}{2}}}{\hbar}\right]\right| \leq 1$$

E is the energy of electrons (holes), V the barrier height (band discontinuity), *m the effective mass of the carriers*, $\hbar$ the Planck's constant divided by 2π, and t_1 and t_2 are the respective well and barrier widths. Since there is no "hard" value for the effective mass of electrons or holes in AlN and GaN, the average values of the available data were taken.[12] The effective mas of electrons was taken as $0.2m_o$ and that of holes as $0.8m_o$. A conduction and valence band discontinuity was chosen by variation to provide the best fit to the transition energies observed by cathodoluminescence. The best fit was obtained when one half of the total bandgap discontinuity (1.4 eV) was assigned to the conduction band and one half to the valence band. The total bandgap discontinuity was calculated as the difference between the bandgaps of AlN and GaN. For the lack of data on the mechanical properties of semiconducting nitrides, the effect of the biaxial strain on the bandgap shift could not be included in the calculation, although it is expected to have a considerable influence on the bandgap of both materials.

The shaded areas in Figure 9(a) represent the lowest four calculated energy bands for the electrons in the conduction band and the holes in the valence band as a function of the individual layer thickness while the thicknesses of the AlN and GaN were kept equal. The lowest transition energy in the superlattice at a particular layer thickness is obtained as the distance between the lower edge of the first energy band for the electrons and the upper edge of the first energy band for the holes. The arrows indicate the transitions in the structures with 1, 3, and 10 nm thick AlN and GaN layers. The length of the arrows corresponds to the emission energy observed by the cathodoluminescence. The luminescence spectra for mentioned three structures are shown in Figure 9(b). The spectra show sharp and well defined peaks with the energies above the bandgap of GaN. The width of the peaks increases with the layer thickness as the superlattice makes a transition from the pseudomorphic to a relaxed structure. The measured and calculated transition energies for these superlattices are collected in Table II.

TABLE II. Calculated and measured transition energies for different layer thicknesses.

Layer thickness [nm]	$E_{calculated}$ [eV]	$E_{measured}$ [eV]	ΔE [meV]
1	4.29	4.11	180
3	3.64	3.47	170
10	3.42	3.42	≈0

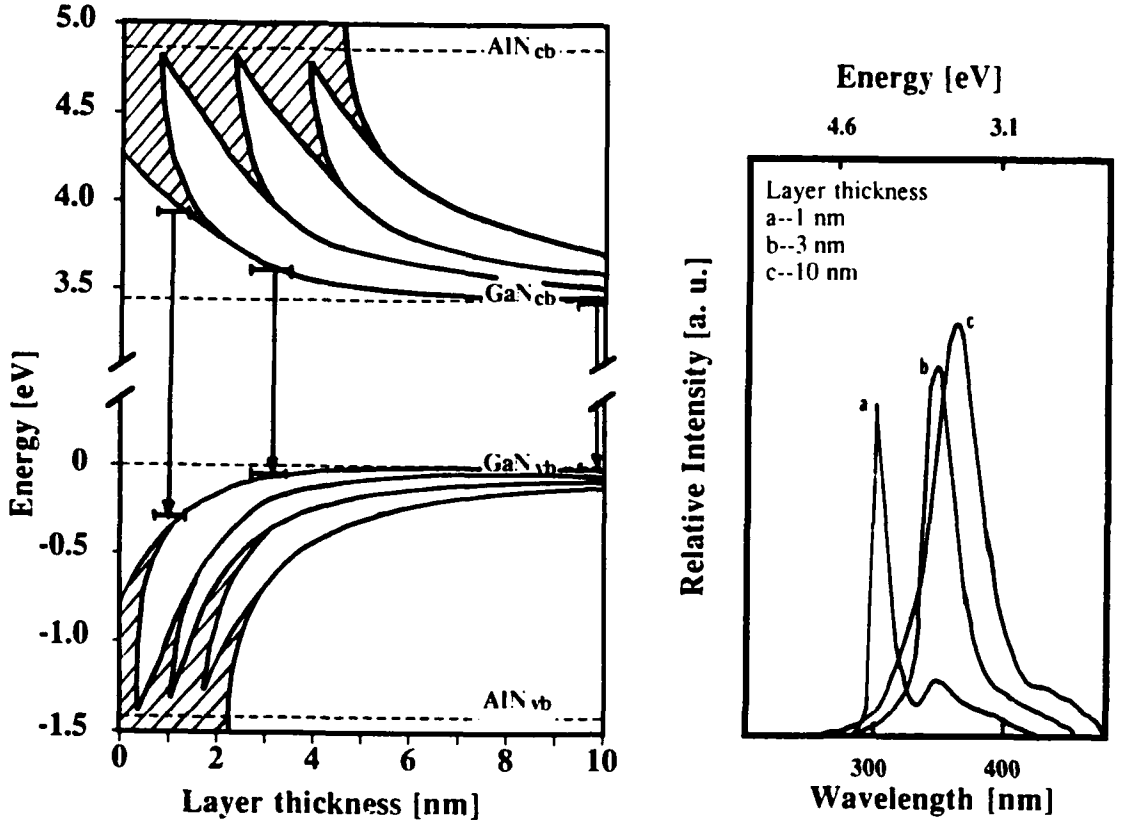

Figure 9: (a) The lowest four calculated energy bands for the electrons in the conduction band and the holes in the valence band as a function of the individual layer thickness while the thicknesses of the AlN and GaN were kept equal. The arrows indicate the transitions in the structures with 1, 3, and 10 nm thick layers, whose cathodoluminescence spectra shown in Fig. 9(b).

Similar to the Figure 9(a), show the shaded areas in Figure U10(a) the lowest two energy bands for the electrons and the lowest three energy bands for holes as a function of the barrier width at a constant well width of 1 nm. The arrows again indicate the measured transition energy of a particular structure. The measured luminescence spectra for 0.5 nm and 1 nm thick barriers are shown in Figure 10(b). The calculated and measured energies are summarized in Table III.

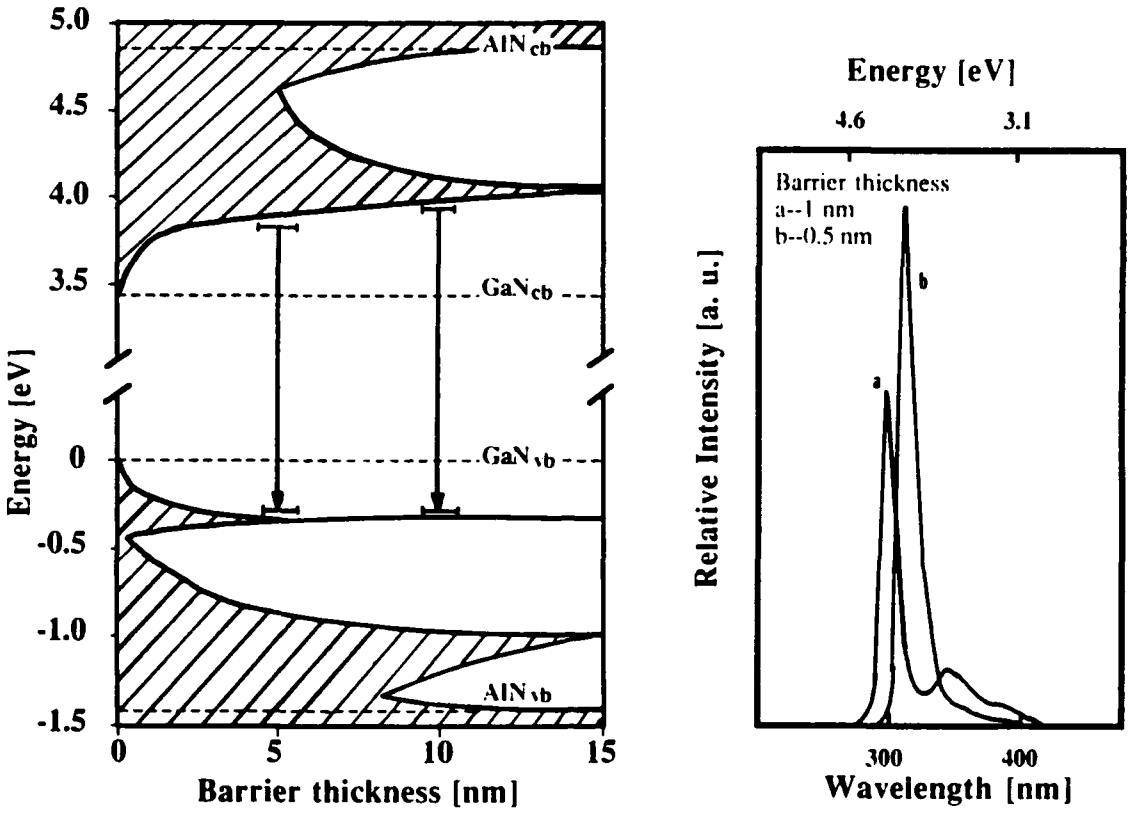

Figure 10: (a) The lowest two energy bands for the electrons and the lowest three energy bands for the holes as a function of the barrier width at a constant well width of 1 nm. The arrows indicate the measured transition energy of a particular structure. The measured luminescence spectra for 0.5 nm and 1 nm thick barriers are shown in Fig. 10(b).

TABLE III. Calculated and measured transition energies for different barrier thicknesses.

Layer thickness [nm]	$E_{calculated}$ [eV]	$E_{measured}$ [eV]	ΔE [meV]
0.5	4.19	3.93	260
1.0	4.29	4.11	180

A quick examination of both tables tells us the following facts: 1) The highest transition energy shift observed in this study was above 700 meV and occurred for the superlattice with 1 nm thick barriers and wells. 2) The emission energy shift for the superlattice with 0.5 nm thick barriers was slightly lower than the value above due to better coupling between adjacent wells (higher tunneling probability due to thinner barriers). 3) There exists an energy offset between the calculated and measured values, which was in the range of experimental error for 10 nm thick layers and increased to 170 meV for thinner layers and even up to 260 meV for superlattices with the thinnest barriers.

The reasons for the observed offset can be several. 1) There exists a possibility that the values for the effective masses used in the calculation are not accurate. For example if the effective masses were larger, one would obtain lower theoretical value for the transition energies and as such also lower offset. 2) The lattice mismatch between AlN and GaN produces strain, which induces bandgap shift in both materials. This shift is expected to be rather high for the materials with 2% misfit (i. e. in the range of ≈100 meV).[13] 3) Interfacial mixing of Al in GaN and Ga in AlN in the monolayer scale could significantly change the transition energy in superlattices having individual layers only a few monolayers thick.

The offset for the moderately thin layers (1 and 3 nm) seems to be fairly constant (180 and 170 meV), which would not be the case if solely an error in the effective masses were in question. The fact, that the offset is negligible for thick layers (layers above the critical thickness, which are relaxed with respect to each other) and almost constant for the layers below the critical thickness (which are biaxially strained) implies the connection between the strain induced bandgap shift and the observed offset. As such luminescence data could be a rough measure whether a layered structure is pseudomorphic or not.

The offset for the superlattices with two monolayer thick barriers is even larger than that of superlattices with moderately thin individual layers for additional 90 meV. This jump, which could not be induced by the strain is most likely the consequence of interfacial mixing, which lowers the barrier height and as such decreases the transition energy. A more sophisticated model, which would include bandgap shift due to elastic strain and also assume one monolayer of interfacial mixing is expected to give much better agreement between the experiment and theory.

III. Boron Nitride

A. Boron Nitride on Silicon Carbide

Overview. Initial attempts to grow c-BN expanded upon the previous approaches by attempting to produce an as-grown, lattice matched, epitaxial c-BN material. The overall experimental objective was the growth of single crystal, cubic gallium nitride[8] (a_0=4.508 Å) films on β-SiC (100) films followed by the growth of a graded composition layer from c-GaN to c-BN and finally a layer of c-BN. If complete solubility exists between c-GaN and c-BN, the final composition should have a lattice parameter sufficiently close to c-BN to produce single crystal thin films of the latter material. In addition, the use of a microwave electron cyclotron resonance (ECR) plasma source provided ion bombardment for formation of the cubic phase.

Growth studies were conducted on in-house produced (100)-oriented cubic β-SiC substrates. A detailed description of the substrate preparation is reported in Reference [17]. The range of conditions used during growth are given in Table VI.

Chemical Analysis. Scanning Auger analysis (JEOL JAMP-30) was performed on each sample to determine the presence of impurities and the nominal composition of the BN layer. Figure 11 is an Auger spectrum taken from the untreated growth surface. The oxygen peak is due to surface oxidation upon exposure to the atmosphere. The carbon peak is often observed to be surface contamination, but is

significant in this case as will be described below. No other contaminants were observed within the resolution of the instrument (typically ≈0.2 at.%).

TABLE IV. Conditions used in GaN-BN growth

Nitrogen pressure	5×10^{-5} – 1×10^{-4} Torr
Microwave power	50 W
Gallium temperature	850 – 990°C
Boron temperature	1500 – 1750°C
Substrate temperature	600 – 700°C
Growth time (BN)	120 – 360 min.
Deposited film thickness	10–850 Å (BN)

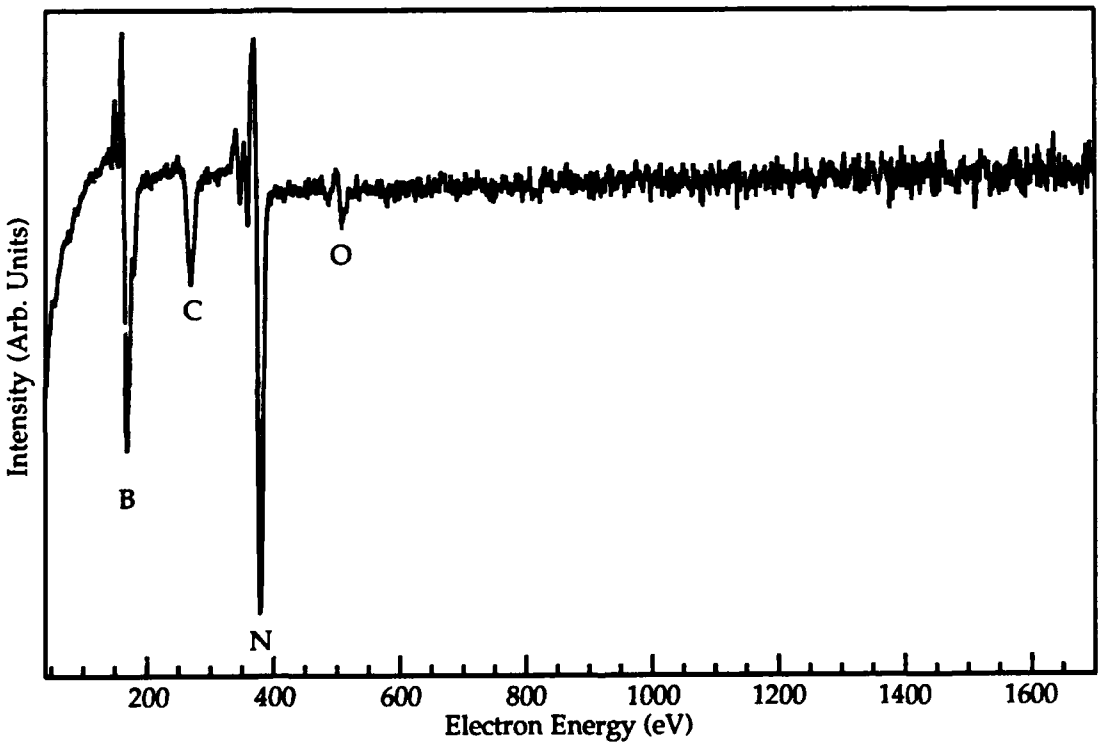

Figure 11. Auger spectra taken from the untreated BN surface. Only oxygen and carbon contamination was detected.

A depth profile was subsequently obtained and is shown in Figure 12. The BN layer thickness is estimated (from SiO_2 sputter rate) to be ≈850Å, while the BN-GaN mixed layer is ≈1000 Å, and the GaN buffer layer is ≈1800Å. The oxygen signal remains near the noise level of the instrument throughout the film and thus is not present in significant concentrations.

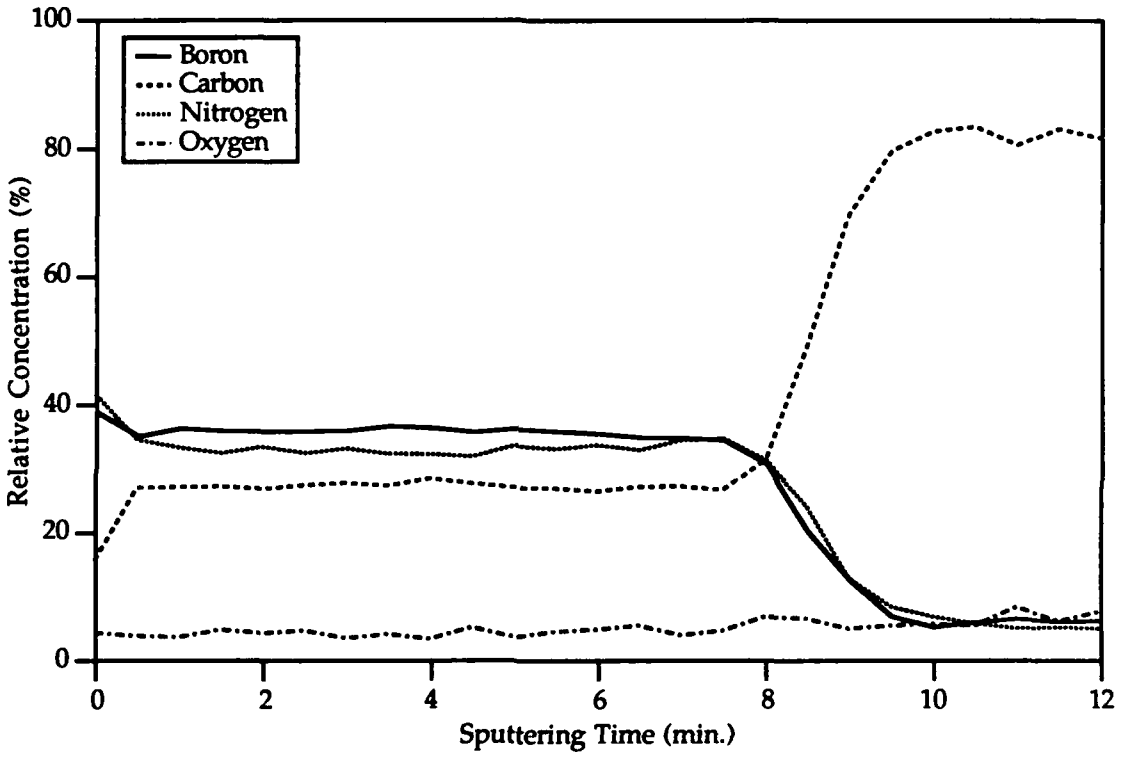

Figure 12. Auger depth profile of the BN layers on β-SiC (100). The profile of the carbon contamination follows that of the boron concentration. The thickness of the BN film is ≈850 Å, and the graded layer is ≈1000 Å.

The depth profile shows that the carbon contamination was significant, and generally followed the boron concentration. After correcting for elemental sensitivities, the B/N ratio is ≈1, despite the high levels of carbon present throughout the layer. The specific source of the carbon contamination is not understood at present, since a number of carbon-free films were grown after a carbon crucible was replaced by one made of pyrolytic BN.

Diagnosis of the source of carbon contamination in the BN films was carried out as follows. A series of samples were grown under a number of different operating conditions and subsequently analyzed by Auger microscopy to identify the conditions that maximized the carbon concentration. It appears now that the carbon is not coming from the high temperature boron effusion cell as previously reported.[18] One source of carbon was identified as being in the incoming nitrogen gas supply. This source was originally discounted, since carbon had not been seen in growths of AlN (which is also a carbide former). However, it appears at present, that boron is a much stronger carbide former as well as being grown at lower growth rates has contributed to its appearance in the BN films. A second gas purifier was installed to reduce the hydrocarbon contamination in the incoming nitrogen gas to <10 ppb levels. Growths shortly after installation showed improvement in the carbon levels, but not elimination. Nearly complete carbon elimination was achieved after repair of the graphite heater stage assembly on the MBE growth manipulator. The exact nature of this mechanism is unknown since carbon diffusion rates are extremely low at the growth temperatures used. It is speculated that some sort of gas phase transport mechanism was involved. The purity of the as-grown film surfaces after both of these modifications were made can be seen from the XPS spectra in Figure 13. It should be noted that this film was actually grown on silicon, but that would not have affected the film purity, especially since the carbon diffusion length at these growth temperatures is nearly zero.

Given the relative purity of the films now produced, an effort was made to quantify the $^{N}/_{B}$ ratio. To get accurate $^{N}/_{B}$ ratios requires that an independent standard be analyzed by the same analytical system used to evaluate the films. To this end a sample of high purity (99.99% min.) pyrolytic BN (Boralloy™, Union Carbide) was obtained. This sample was analyzed by our XPS system and resulted in a relative $^{N}/_{B}$ sensitivity factor of 3.68, which is very close to the value of 3.70 published by Surface Science Laboratories, Inc.

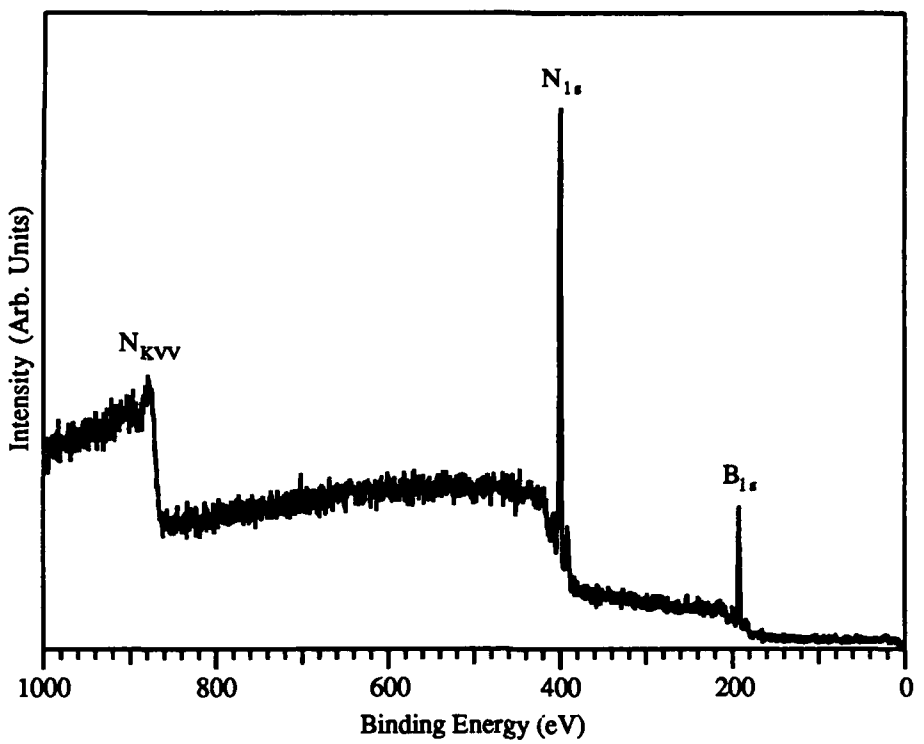

Figure 13. XPS spectra (Mg anode) of BN film grown after removal of carbon sources previously active during growth.

With this ratio, the stoichiometry of the now relatively pure films was accurately calculated. The film shown in Figure M3 gives a $^{N}/_{B}$ ratio of 1.21, indicating that there is a large excess of nitrogen at the film surface. It is unknown at present how this nitrogen excess is incorporated in the film, but it might play an important role in the present amorphous nature of these films. Furthermore, additional AES studies showed that there was still a small amount (roughly <1% level) of carbon and oxygen in the films. Remaining impurity levels should be eliminated when the substrate heater is replaced with an encapsulated pyrolytic graphite heater.

Structural Analysis. Reflection high-energy electron diffraction performed during growth indicated that the BGaN film remained predominantly single crystal, but shows both a normal cubic [110] pattern and a second hexagonal pattern [01$\bar{1}$0]. By contrast, during the deposition of the BN, the RHEED pattern indicated that this film was predominantly amorphous with some microcrystallinity also present.

Transmission electron microscopy (TEM) was used (Hitachi H-800) to more closely examine the microstructural evolution of the BN/BGaN/GaN epitaxial films. Cross-section TEM specimens were prepared using standard techniques described in Reference [19]. Examination in bright-field and with selected area diffraction (SAD) also showed the BGaN layer to be a mixture of cubic and wurtzitic phases. This layer was heavily faulted. The latter phenomenon is to be expected given the high degree of lattice mismatch (19.8%) being accommodated in a layer of only 1000 Å. Examination of the diffraction patterns taken from the BN film revealed this layer to be amorphous, as shown in Figure 14. Only the top film of the multilayer assembly is shown (a-BN), which displays a contrast similar to the epoxy. The BGaN layer is nearly opaque because its lower ion milling rate left it much thicker than the BN layer.

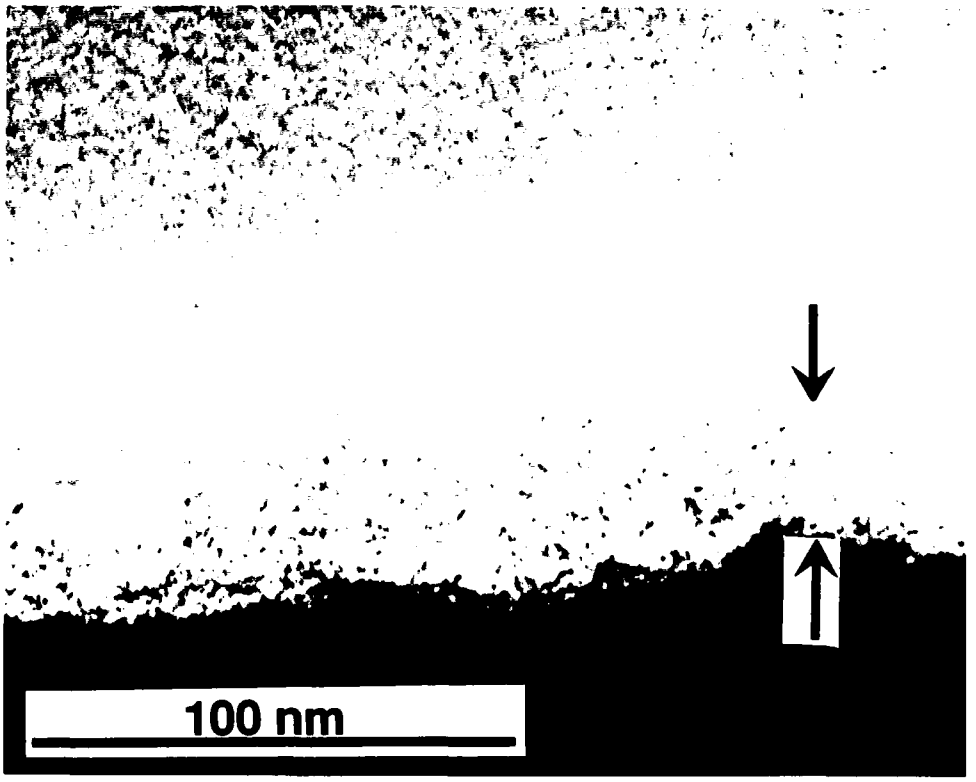

Figure 14. XTEM photograph (z=[110]) of the top of the deposited film with the BN marked. The low contrast of the layer is due to its amorphous nature (see text).

SEM examination of the surface of the film was performed to evaluate the surface morphology produced during the deposition. The resulting morphology was quite good as can be seen in Figure 15.

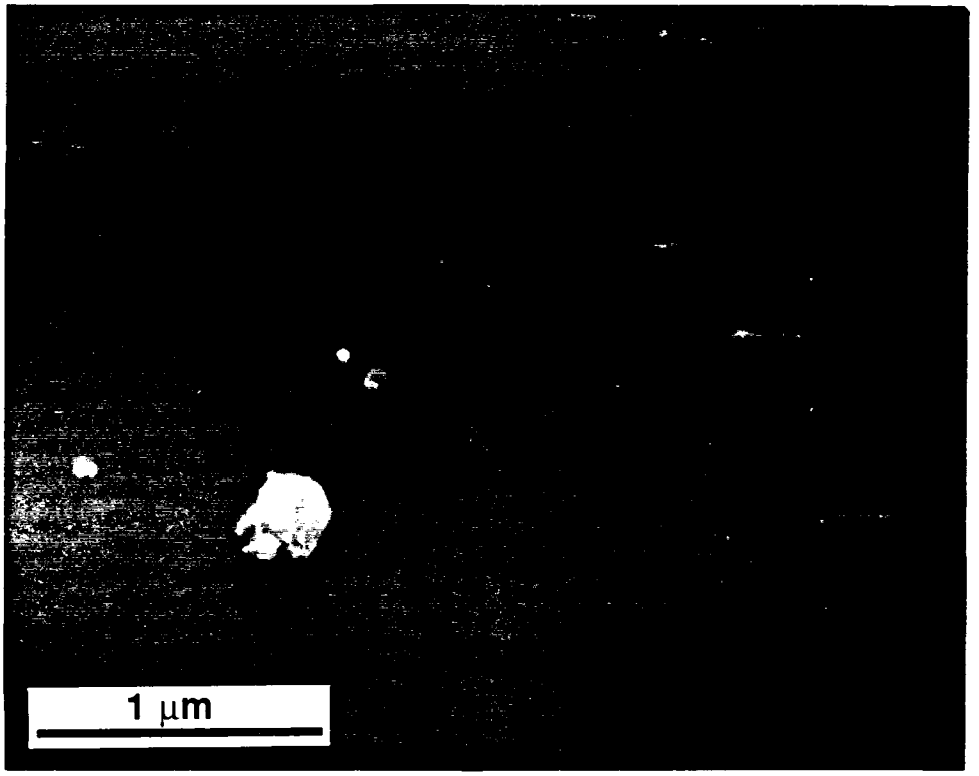

Figure 15. SEM photograph of the surface of the deposited film. The white particles on the surface appear to be contaminants that adhered after the samples exposure to the atmosphere.

B. Boron Nitride on Diamond (100)

Diamond (100) substrates (4 mm × 4 mm × 0.25 mm, type IIa) were purchased from Dubbledee Harris Diamond Corp., in an attempt to grow c-BN (100) layers on it. Diamond makes a nearly ideal substrate for c-BN, due to its low lattice mismatch (≈1.4%) and higher surface energy, which both promote two-dimensional growth.

The diamond substrates were degreased in a series of organic solvents (trichloroethylene, acetone, methanol and ethanol) to remove hydrocarbon residues. Subsequent examination in a field emission SEM (Hitachi S-4000) revealed a rough surface morphology, which is shown in Figure 16.

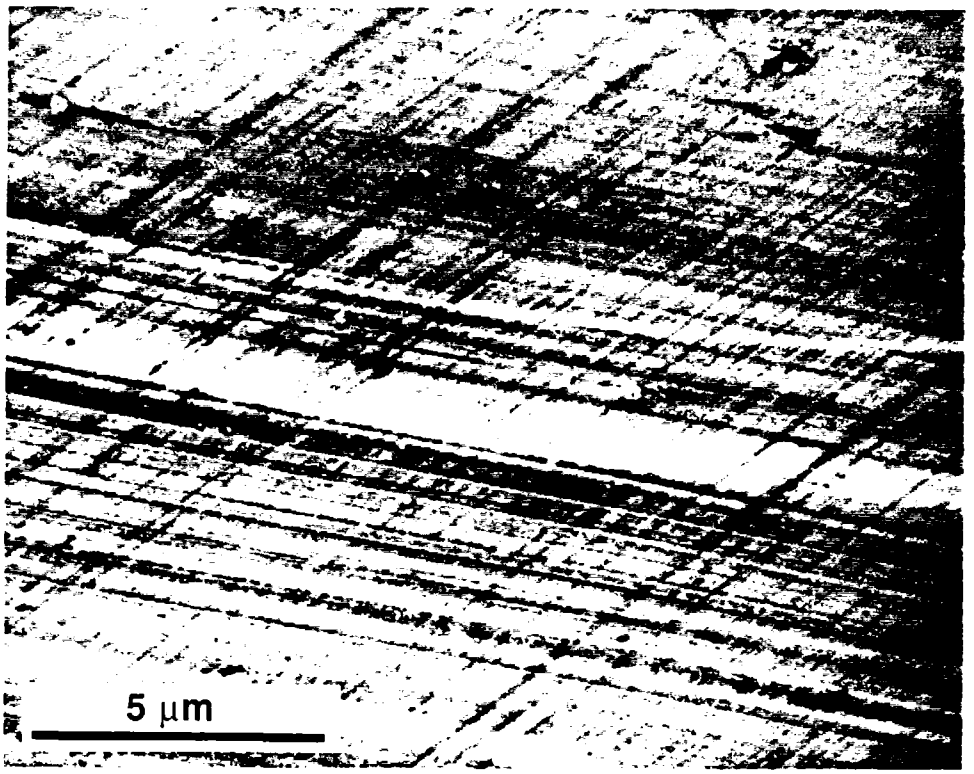

Figure 16. Scanning electron microscope photograph of the unetched but thoroughly degreased diamond surface. Note the appearance of the polishing scratches in conjunction with a dark carbonaceous or hydrocarbon-like deposit.

After these investigations, it became apparent that the polishing procedures might well leave graphitic and/or highly damaged diamond layers on the surface which would in turn interfere with the proper initiation of c-BN growth on its surface. Thus, a graphite etching procedure reported in the literature[20] was added to the substrate preparation procedures. This etch involves soaking for 45 min. in a heated solution of H_2SO_4:HNO_3:$HClO_4$ in the proportions 3:4:1. Figure 17 shows the the surface morphology produced by this procedure.

Note that polishing artifacts are much less pronounced in this micrograph, but a heavily stepped surface was revealed by the etching procedure. It would appear that there was a substantial graphitic or damaged layer present which was removed by the etchant. The highly stepped surface, while not a major obstacle for current growth

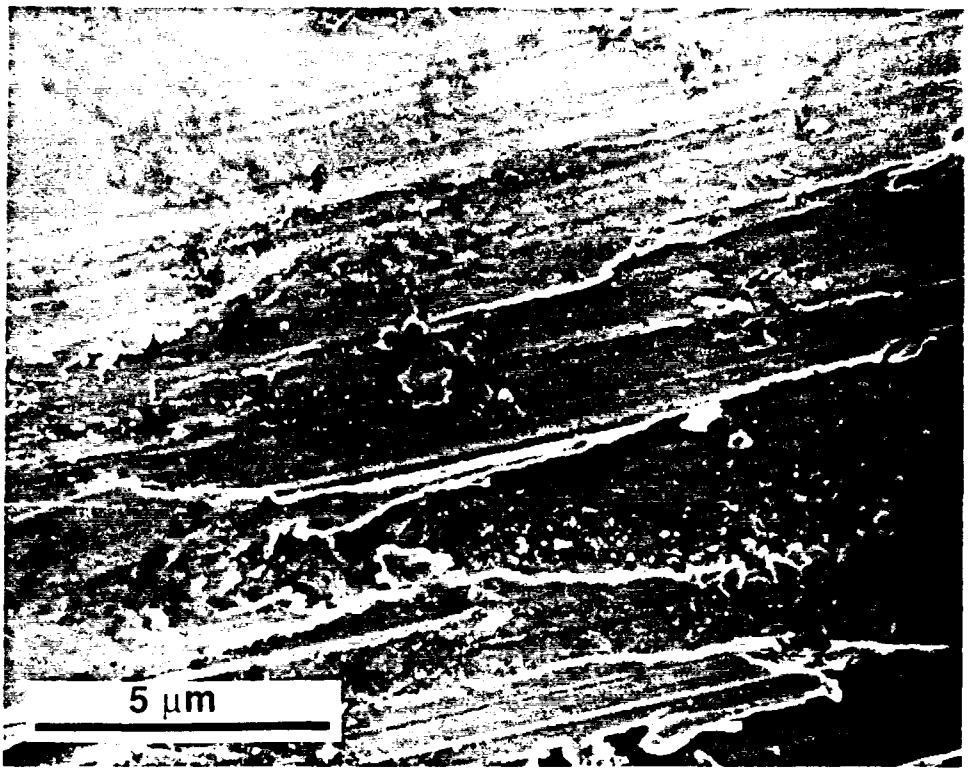

Figure 17. Scanning electron micrograph of the diamond surface after an oxidizing etch to remove graphitic layers.

studies, does pose a serious problem for future research involving device development.

As a result, discussions were held with representatives of Dubbledee Harris Diamond Corp. and their European supplier regarding these findings resulted in a commitment by them to perform additional quality control tests on the next shipment of diamond substrates. When these new substrates arrive, the same tests will be performed in our laboratories to provide verification of their results. These strenuous evaluation procedures will hopefully result in higher quality diamond substrates for this as well as future studies.

After the cleaning and etching procedures were completed, the diamond samples were rinsed in DI water and dried and then mounted onto a silicon wafer using a commercial ceramic adhesive (Ceramabond™ 503, Aremco Products, Inc.). The silicon wafer was then indium bonded to the molybdenum MBE substrate block.

This procedure was used to avoid indium diffusion onto the diamond surface, which readily occurs on 0.25 mm α-SiC substrates.

The substrates were then loaded into the MBE system and degassed to 800°C. Higher temperatures for degassing which are typical for silicon processing were not used to avoid graphitizing the surface in the UHV conditions. Typical growth conditions are shown in Table V.

TABLE V. Conditions used in BN on diamond growth

Nitrogen pressure	1×10^{-4} Torr
Microwave power	50 W
Boron temperature	1500 – 1750°C
Substrate temperature	400 – 700°C
Growth time	120 – 480 min.
Deposited film thickness (approx.)	10–1100 Å

After growth the samples were removed and evaluated using x-ray diffraction. AES was not performed due to the charging of the film/substrate. XPS was also not done due to difficulties with the small sample size, though it would be expected that the composition of the film would not differ from that observed on other substrates. X-ray diffraction indicated that the films were a mixture of graphitic and cubic BN. Interestingly, it appears that the c-BN present was oriented to the substrate, since only the (400) and (200) peaks from the c-BN were observed (see Figure 18), which would not be possible if it were randomly oriented. This is because the c-BN (220) and (111) are stronger reflections, 3X and 50X, respectively, than the observed (200) reflection. Therefore, crystals in these orientations would have been easily observed, even in relatively smaller fractions of the deposited film.

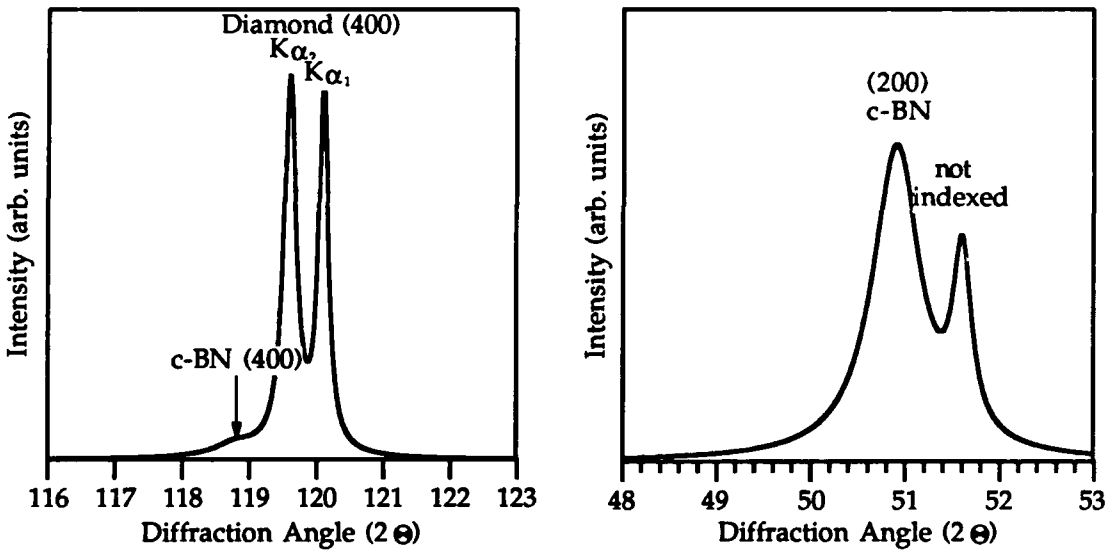

Figure 18. X-ray spectra ($Cu_{K\alpha}$) of BN on diamond. (Left) Diamond and c-BN (400) reflections. (Right) c-BN (200) reflection, since diamond (200) is forbidden by the structure factor.

C. Laser Ablation

Work has begun on laser ablation of BN targets to deposit cubic BN films. This work is being done in collaboration with A. F. Schreiner in Chemistry and O. H. Auciello in Materials Science and Engineering, both of NCSU. The technique involves the use of a pulsed ArF laser (λ=193 nm) passing through a special UV-grade quartz window into a UHV chamber where it strikes a BN target. The target ablates under the high energies imparted by the laser pulse and are subsequently deposited on a substrate. A quartz crystal deposition monitor is mounted in the ablation path to permit monitoring of the deposition thickness and rate.

It is thought that the activated material ejected from the surface may provide the necessary energy to allow the depositing BN to crystallize on the substrate in the cubic phase. This is supported by Doll *et al*[21], who deposited c-BN layers on silicon and the fact that polycrystalline TiN has been deposited on a room temperature substrate via laser ablation. The system also has facilities for heating the substrate as well.

TABLE VI. Conditions used in BN laser ablation on silicon growth

Nitrogen pressure	$1\times10^{-4} - 3\times10^{-2}$ Torr
Average laser power	0.1–0.55 W
Laser pulse	20 ns @ 10 pulse/sec
Substrate temperature	400 – 600°C
Total overall growth time (typical)	120 min.
Deposited film thickness (approx.)	50–500 Å (BN)

Results from preliminary depositions were mixed. The deposition rate was quite high initially, but then dropped rapidly to zero. Concurrently, a dark rectangular stripe appeared on the surface of the target, corresponding to the shape of the excimer laser cavity. This deactivation was also observed by Doll *et al*[21] when using a KrF laser (λ=248 nm). It is speculated in the case of ArF that the BN was decomposing and ablating, which would quickly produce a boron-rich phase that would resist further ablation. By moving the target to an unimpacted region, the deposition could be slowly continued, until after several hours, a layer 200 Å thick was produced. At this point, the target was sufficiently affected to effectively prevent further deposition, and so the substrate was removed for analysis.

X-ray diffraction was performed and a typical spectra is shown in Figure 19. Note that while a number of peaks were observed for hexagonal and wurtzitic BN, no peaks were observed for the cubic phase.

It is unclear at present for the lack of the c-BN phase, though perhaps the higher photon energy of the ArF laser results in processes which are more favorable to the formation of w-BN. Additional x-ray diffraction was performed on the h-BN targets, on both the laser impacted material and the unaffected areas. Figure 20 shows the comparison of these two areas on the target.

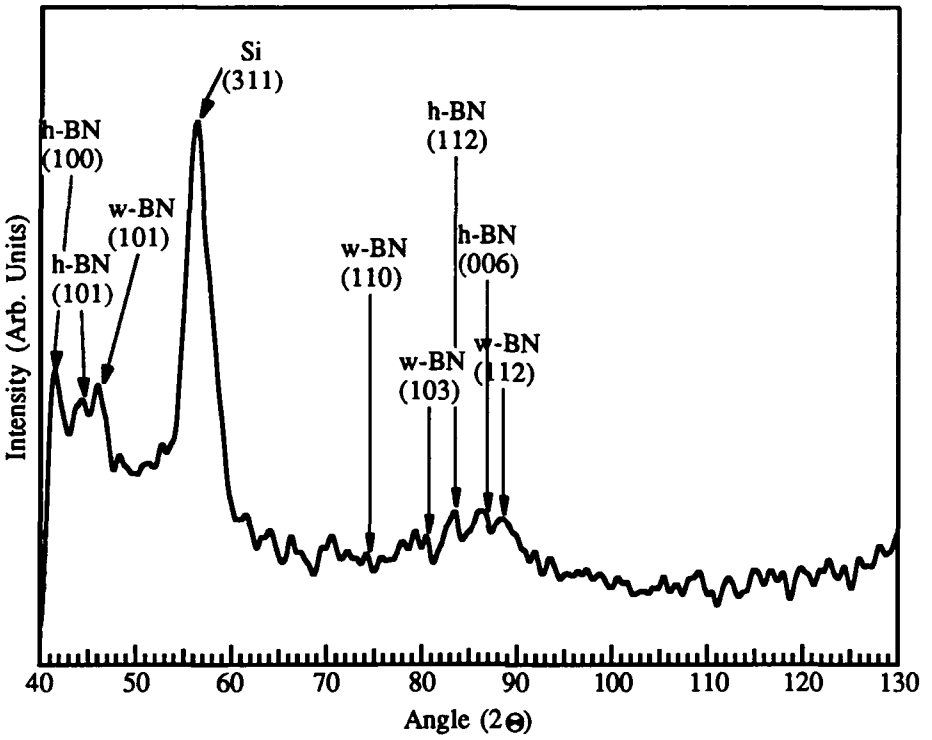

Figure 19. X-ray diffraction spectra ($Cu_{K\alpha}$) of Si (100) target after laser ablation. Film thickness measured during deposition via quartz crystal monitor is 525 Å.

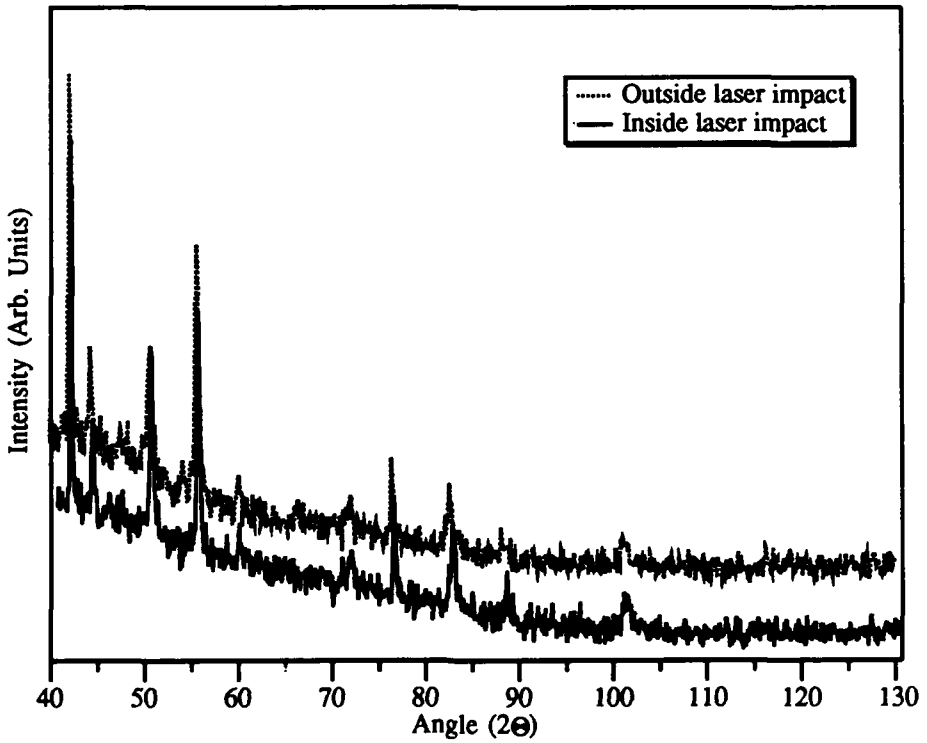

Figure 20. X-ray powder diffraction patterns ($Cu_{K\alpha}$) of hexagonal BN target inside and outside laser ablated area. Diffraction peaks are not indexed since all peaks are from h-BN.

There was no evidence in the diffraction pattern of any residual cubic or wurtzitic BN crystals. Small amounts would be expected, and have been observed in other cases.[22] This is true especially since the laser develops an area which will no longer ablate, and so reduces the energy applied to the target, allowing an intermediate energy input which might convert material without ablating it.

Auger electron spectroscopy showed that a slightly sub-stoichiometric BN layer was deposited on the Si substrate. It also showed a small amount of Ca, which is likely due to purity of the target, since it was a hot-pressed product, and Ca is a typical sintering agent. Surprisingly, AES of the target did not show discernable composition differences between the light (unexposed) and dark (ablated) areas, which were clearly visible in the Auger microscope. Clear differences in the boron peak shape were observed, however. This somewhat anomalous result is under investigation.

D. Characterization of Sumitomo c-BN

Work has also been done on the characterization of polycrystalline c-BN substrate materials obtained from Sumitomo Electric in Japan. Figure 21 is shows a surface electron energy loss spectroscopy (EELS) plot of the surface of the substrate.

The plasmon loss features are evident and are similar to spectra taken by transmission EELS done by Hosoi *et al*[23] The unsputtered spectra on the left shows peaks at 23 and 35 eV. Hosoi *et al* observed a 33 eV feature which was attributed by them to be to a $\sigma \rightarrow \sigma^*$ plasmon transition in w-BN. They observed 25 and 26 eV features which they attributed to $\pi+\sigma$ transitions in amorphous and h-BN. Since our spectra might have been affected by substrate polishing and oxidation or other artifacts from surface treatments, the sample was sputter cleaned and annealed.

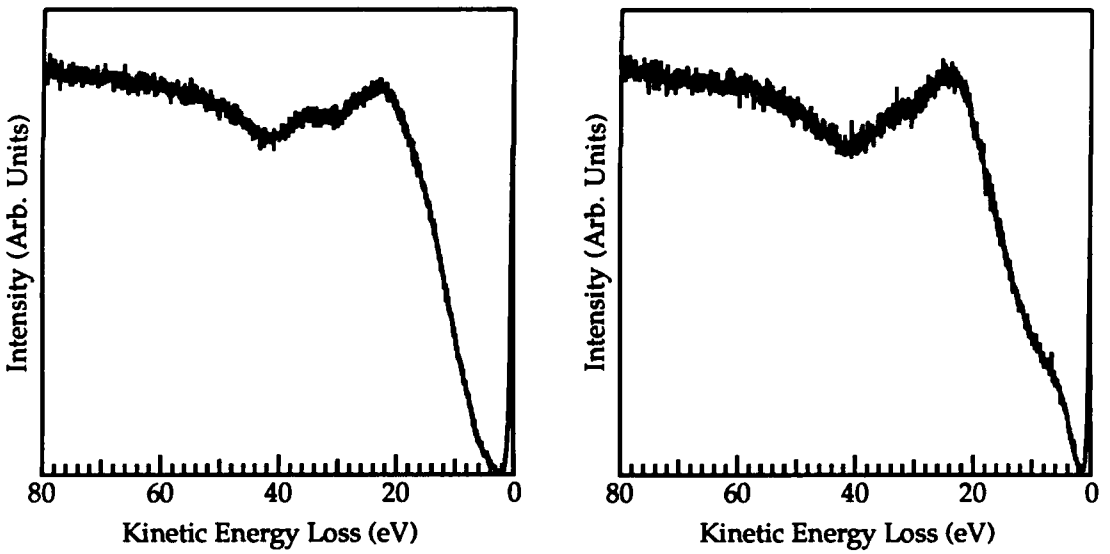

Figure 21. Surface EELS spectra (E_p=1000 V) of polycrystalline c-BN sample obtained from Sumitomo Electric Corporation. Left graph shows as received spectra and right graph shows after 3 kV Ar^+ sputter clean followed by 900°C anneal.

The right spectra in Figure 21 shows the plasmon loss features after the annealing. The 33 eV feature is reduced and the 23 eV feature has been shifted up to 26 eV, much closer to the 29 eV peak that Hosoi *et al* observed for the $\sigma \rightarrow \sigma^*$ plasmon transition in c-BN. However, an additional feature has appeared around 9 eV which Hosoi *et al* attributed to a $\pi \rightarrow \pi^*$ plasmon transition in h-BN. Thus, it appears that the sputter clean did remove the most but perhaps not all of the surface artifacts, but added a small amount of h-BN. It is not surprising that a relatively low temperature anneal (for BN) of 900°C would be unable to completely reorder the surface. Thus, it appears that spectra of these substrates can then be used as reference standards to characterize the cubic nature of BN films deposited in the MBE system.

One final characterization of the Sumitomo substrates involved examination of the surface via SEM. Shown in Figure 22 is an SEM photograph of the c-BN surface observed.

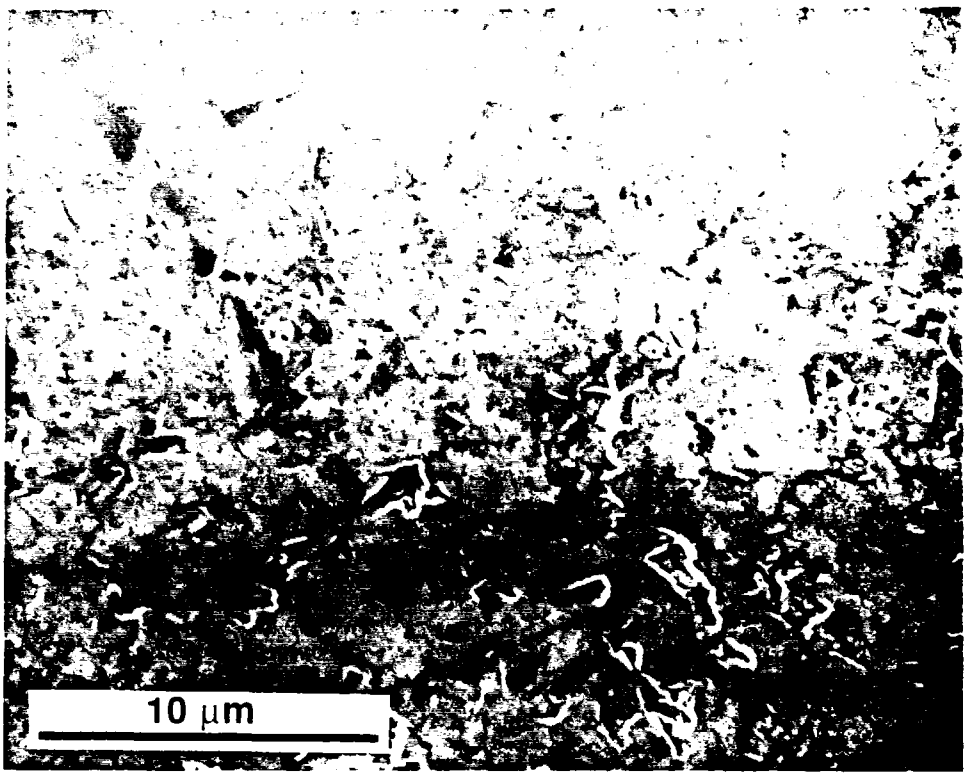

Figure 22. Scanning electron microscope photograph of surface of Sumitomo polycrystalline c-BN substrates.

The surface of the c-BN substrates is quite rough, showing angular pits distributed all over the surface. This is very likely due to the extreme hardness of the c-BN, making polishing extremely difficult. These pits also explain why the sputter cleaning on the EELS sample did not remove all of the surface treatment artifacts. A rough surface would be very much harder to sputter clean than a smooth one, due to shadowing effects. In conclusion, it remains for future investigation to determine if these substrates will be appropriate for use in growth studies, though they have been useful in characterization studies of c-BN.

E. Future Research

Gas Source MBE. The first problem to address is the hyperstoichiometric BN films. Reduction of the stoichiometry is speculated to play a role in the present amorphous nature of the films. Two solutions to this problem might be: (1) increasing the boron flux rate to provide boron atoms for the excess nitrogen to bond, and

(2) increasing the substrate temperature to provide mobility for the excess nitrogen to diffuse to the surface and be desorbed. The related problem of low levels of remaining contaminants should be eliminated when the heater stage is replaced.

Another approach involves the use of the use of an alternative boron source such as borazine ($B_3N_3H_6$) in the gas-source MBE system and activated in the ECR plasma. This reactive species has been used by several investigators[24–29] for production of BN films. The resulting films have usually had moderate-to-high concentrations of c-BN, especially in cases where plasmas were used. This will be the first use borazine with an ECR source, however. The structure of the borazine molecule is shown in Figure 23; the properties of this materials are given in Table VII.

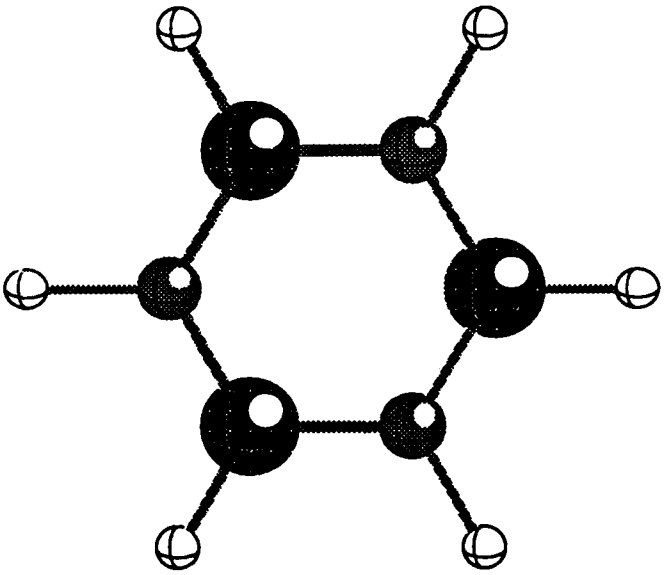

Figure 23. Diagram of a borazine ($B_3N_3H_6$) molecule, which is isoelectronic and nearly isostructural with benzene (C_6H_6). In addition, there is likely a slight three-dimensional rumpling of the molecule (not shown).

TABLE VII. Important properties of borazine
(From Callery Chemical Co. literature)

Formula:	$B_3N_3H_6$
Molec. Wt.:	80.51
Form:	Colorless liquid at room temperature
Structure:	Non-planar six-membered ring. Isoelectronic with benzene.
B–N bond:	1.4355 Å
B–H bond:	1.259 ± 0.019 Å
BNB angle:	117.7°±1.2°
NBN angle:	121.1°±1.2°
Melting Point:	–56.2°C
Boiling Point:	55°C
Vapor Pressure:	log (Pmm) = –1609/T(K) +7.714
Density:	1.00 g/ml @ MP, 0.81 g/ml @ 55°C
Heat Vaporization:	7.0 kcal/mol
Heat of Formation:	–131.1±3.2 kcal/mol (liquid) and –124.1±3.2 kcal/mol (gas)
Safety Data:	Low flash point (<35°F) material. Very corrosive as well. TLV and related human exposure data unavailable, though asssumed very toxic due to possible reaction byproducts. Unstable above 0–5°C, slowly decomposes into long chain molecules.

Laser Ablation. Work will also continue in other growth technologies for c-BN layers. The laser ablation of a hexagonal BN target with an ArF laser will be extended to the use of a KrF laser (λ=248 nm) based on the work of Doll *et al.*[21] They were able to produce c-BN films that were in a preferred orientation to the Si (100) substrates which would seem to have minimal misfit, despite the 33% mismatch in lattice parameter. The orientation observed was c-BN(100)||Si(100) and c-BN⟨001⟩||Si⟨011⟩. This orientation presents to the growing c-BN layer a periodicity of $(1/\sqrt{2} \times 1/\sqrt{2})$R45°, which is shown below. Note that the new periodic "net" is shown displaced in the figure and located in the next growth sites available above the Si (100) surface.

This new lattice is 6% larger than c-BN, which Doll *et al* cited to explain why they observed a lattice parameter of 3.8 Å, rather than 3.62 Å. The c-BN layer was able to expand to accommodate nearly all of the distortion required.

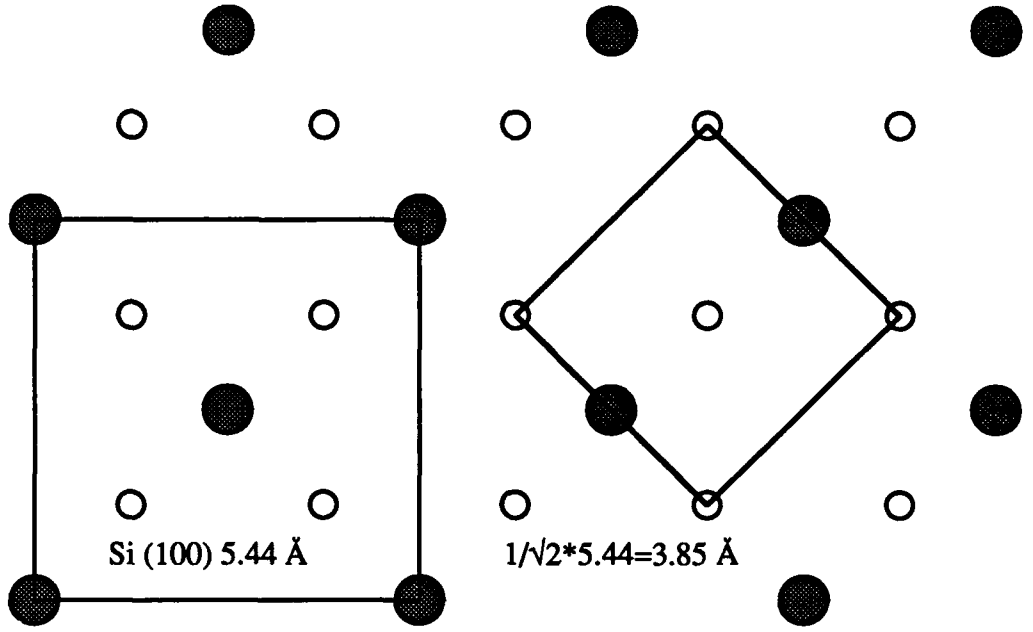

Figure 24. Schematic diagram of Si (100) face, showing the periodicity of $(1/\sqrt{2} \times 1/\sqrt{2})R45°$ possible on this face, displaced upward to the next growth location above the Si surface.

Additional wavelengths are also possible with this laser system and might be investigated, should they prove to be strongly absorbed by graphitic BN. Table VIII shows the wavelengths possible in this system.

TABLE VIII. Some of the laser wavelengths possible in NCSU system.

Gas	Wavelength	Energy
F_2	157 nm	7.90 eV
ArF	193 nm	6.42 eV
KrCl	222 nm	5.59 eV
KrF	249 nm	4.98 eV
XeCl	308 nm	4.03 eV
N_2	337 nm	3.68 eV
XeF	350 nm	3.54 eV
N_2^+	428 nm	2.90 eV
F	624–780 nm	1.99–1.59 eV
CO_2	10,600 nm	0.117 eV

Analytical Techniques. Due to the difficulty of preparing diamond and c-BN samples for examination by TEM, other techniques will need to be heavily relied upon for initial diagnostic information on the crystalline nature and quality of the c-BN films produced. The current x-ray diffractometer has proven to be quite difficult to use with the small single crystal diamond substrates and the resulting oriented films, due to its lack of a goniometer stage.

Work is currently underway to recommission a diffractometer in the laboratories of Klaus Bachmann, in the Materials Science and Engineering department at NCSU. This system is a triple crystal diffractometer with a goniometer stage, which will permit accurate alignment of the substrate crystal. Thus, measurement of the individual peaks will be much easier to obtain. In addition, since the x-rays in this system are extremely monochromatic, rocking curves will be possible to measure the strain present in the films.

Further work will continue in the development of additional techniques for analyzing c-BN films. Further EELS studies will determine how effective that technique will be in observing h-BN and c-BN features. Arrangements have also been made to have samples analyzed using Raman spectroscopy and/or micro-Raman spectroscopy in the laboratories of Dr. Robert Nemanich in the Physics Department here at NCSU.

IV. References

1. R. F. Davis, Z. Sitar, B. E. Williams, H. S. Kong, H. J. Kim, J. W. Palmour, J. A. Edmond, J. Ryu, J. T. Glass, and C. H. Carter, Jr., Mat. Sci. & Eng. B1, 77 (1988).

2. P. M. Dryburgh, J. Cr. Growth 94, 23 (1989).

3. Y. Koide, H. Itoh, M. R. H. Khan, K. Hiramatu, N. Sawaki, and I. Akasaki, J. Appl. Phys. 61, 4540 (1987).

4. W. T. Tsang, Appl. Phys. Lett. 39, 786 (1981).

5. M. G. Burt, Electron. Lett. 19, 210 (1983).

6. P. Davson, G. Duggan, H. I. Ralph, and K. Woodbridge, Superlattices and Microstr. 1, 173 (1985).

7. N. Holonyak, Jr., R. M. Kolbas, R. D. Dupuis, and P. D. Dapkus, IEEE J. Quantum Electron. QE16, 170 (1980).

8. M. J. Paisley, Z. Sitar, J. B. Posthill, and R. F. Davis, J. Vac . Sci. Technol. A 7, 701 (1989).

9. Z. Sitar, M. J. Paisley, D. K. Smith, and R. F. Davis, submitted to Rev. Sci. Instr.

10. J. C. Bravman and R. Sinclair, J. Electron Microsc. Tech. 1, 53 (1987).

11. M. Quillec, L. Goldstein, G. Le Roux, J. Burgeat, and J. Primot, J. Appl. Phys. 55, 2904 (1984).

12. B. L. Jiang, F. Shimura, and G. A. Rozgonyi, Appl. Phys. Lett. 52, 1258 (1988).

13. C. Delamarre, A. Dubon, J. Y. Laval, B. Guenais, and J. Y. Emery, *Semiconductor Quantum Well Structures and Superlattices*, Mat. Res. Soc. Europe Proc. VI,edited by K. Ploog and N. T. Linh, Strasbourg, France, 105 (1985).

14. D. A. Andrews, R. Heckingbottom, and G. J. Davies, *Semiconductor Quantum Well Structures and Superlattices*, Mat. Res. Soc. Europe Proc. VI,edited by K. Ploog and N. T. Linh, Strasbourg, France, 85 (1985).

15. For example; R. L. Liboff, *Introductory Quantum Mechanics*, Holden–Day, Inc., San Francisco (1980).

16. R. C. DeVries, *Cubic Boron Nitride: Handbook of Properties*, Technical Information Series, General Electric Company, Corporate Research and Development, Report #72CRD178, 1972.

17. M. J. Paisley, Z. Sitar, J. B. Posthill, and R. F. Davis, *Journal of Vacuum Science and Technology A*, Vol. 7, No. 3, pp. 701–5 (1989).

18. M. J. Paisley, Z. Sitar, C. H. Carter Jr., and R. F. Davis, in SPIE's OE/LASE—Innovative Science and Technology Symposium, Carl. A. Kukkonen, Vol. 877, pp. 8–12, SPIE-The International Society for Optical Engineering (Los Angeles, CA, 1988).

19. M. J. Paisley, Z. Sitar, Benda Yan, and R. F. Davis, *Journal of Vacuum Science and Technology B*, Vol. 8, No. 2, pp. 323–6 (1990).

20. J. C. Bravman, and R. Sinclair, *Journal of Electron Microscopy Technique*, Vol. 1, pp. 53 (1984).

21 Johan F. Prins, *Journal of Physics D*, Vol. 22, pp. 1562–4 (1989).

22. G. L. Doll, J. A. Sell, L. Salamanca-Riba, and A. K. Ballal, in Proceedings of the Spring 1990 Meeting of the Materials Research Society, J. T. Glass, ed., preprint (Boston, MA, 1990).

23. M. Sokolowski, A. Sokolowska, M. Wronikowski, and T. Kosik, *Journal of Materials Science*, Vol. 25, No. 1a, pp. 263–7 (1990).

24. Jun Hosoi, Tetsuo Oikawa, Masao Inoue, Yoshio Matsui, and Tadashi Endo, *Journal of Electron Spectroscopy and Related Phenomena*, Vol. 27, pp. 243-254 (1982).

25. Kazuhisa Miyoshi, Donald H. Buckley, and Talivaldis Spalvins, *Journal of Vacuum Science and Technology A*, Vol. 3, No. 6, pp. 2340–4 (1985).

26. Kazuhisa Miyoshi, Donald H. Buckley, John J. Pouch, Samuel A. Alterovitz, and Harold E. Sliney, *Surface and Coatings Technology*, Vol. 33, pp. 221–33 (1987).

27. A. C. Adams, *Journal of the Electrochemical Society*, Vol. 128, No. 6, pp. 1378–9 (1981).

28. Ward Halverson and Dennis T. Quinto, *Journal of Vacuum Science and Technology A*, Vol. 3, No. 6, pp. 2141–6 (1985).

29. S. Shanfield and R. Wolfson, *Journal of Vacuum Science and Technology A*, Vol. 1, No. 2, pp. 323–5 (1983).

30. J. Kouvetakis, V. V. Patel, C. W. Miller, and D. B. Beach, *preprint*, (1990?).

Appendix: Electron Cyclotron Resonance (ECR) Plasma Source

A.I. Introduction

Electron cyclotron resonance (ECR) plasma sources provide a denser plasma compared to radio frequency (rf) or conventional microwave sources and operate over a much larger pressure range. These sources use a magnetic field which simultaneously causes electrons to move in circular orbits and confines the plasma. When the orbital frequency of the electrons, $\nu = \frac{eB}{2\pi m_o}$, equals the frequency of electromagnetic radiation used for plasma excitation, resonance occurs, and the electrons absorb electromagnetic radiation more efficiently. For the microwave frequency of 2.45 GHz, resonance occurs when the magnetic field density equals to 875 Gauss.

Two distinctive types of ECR plasma sources have been developed: axial[A-1] and distributed (or multicusp)[A-2, A-3]. In the former one or two electromagnetic coils are used for the formation of the axial magnetic field, necessary for resonance and for the formation of a magnetic mirror. By comparison several rare earth magnets are used in the latter source for the formation of a multipolar magnetic field.

At present, the principal areas of application for these sources are plasma enhanced chemical vapor deposition (PECVD)[A-4–A-6] and reactive ion etching (RIE)[A-7–A-8]. At the outset of this developmental research program all available ECR plasma sources were large in diameter (usually 15–20 cm) such that they could not be accommodated within commercial molecular beam epitaxy (MBE) equipment.

We designed and commissioned the first compact, ultra-high vacuum compatible ECR plasma source which fits completely into the sleeve of a standard MBE effusion cell (2.25" diameter). This enables positioning of the source behind the shutter, thus providing the same source-to-substrate distance as for effusion cells. This eliminates unwanted collisions of active species with the walls of the system which act as recombination sites. The basic design employs a coaxial microwave

cavity surrounded by three electromagnets which produce the resonant, mirror, and extraction magnetic fields. The source is operated at low power (from a few to 120 W) which makes the external microwave system very simple, i.e., no circulators, dummy loads, or nonflexible waveguides are needed.

This source was initially designed for the deposition of III–V nitrides in an MBE environment, which was carried on at low temperatures, 400–600°C, using molecular nitrogen. In addition to the growth of nitrides, this source also has potential for production of active oxygen. The later species may be used for low temperature deposition of high T_c superconductors, as well as, for the decomposition of various molecular gases (e. g. organometallics) and for *in–situ* substrate cleaning prior to deposition.

A-II. Description of the NCSU–ECR Plasma Source

Source head. A cross-sectional diagram of the source is shown in Figure A-1. Microwaves (2.45 GHz) are introduced into the vacuum through an N-type, 50 Ω coaxial feedthrough (1), welded on a standard 1.33" Conflat® flange which provides a UHV seal and simple assembly and disassembly. The feedthrough is attached to the plasma chamber (2), which is made of nonmagnetic stainless steel, having an inner diameter of 23 mm. This dimension is much too small for a circular waveguide to transmit or to be excited at 2.45 GHz. The critical diameters for an empty circular waveguide at this frequency for the operation in TM_{01} or TE_{11} mode are 94 mm and 72 mm, respectively. In order to overcome this problem a coaxial structure (3) was designed with a shell-to-inner conductor radius ratio of 2.3, which continues the existing 50 Ω line impedance and minimizes reflected power at the transition from the feedthrough to the microwave antenna (4). In order to prevent discharge at the feedthrough, the back end of the source was filled with an insulator (5) made of hot–pressed boron nitride.

® A registered trade mark of Varian Associates, Inc., Lexington, MA 02173

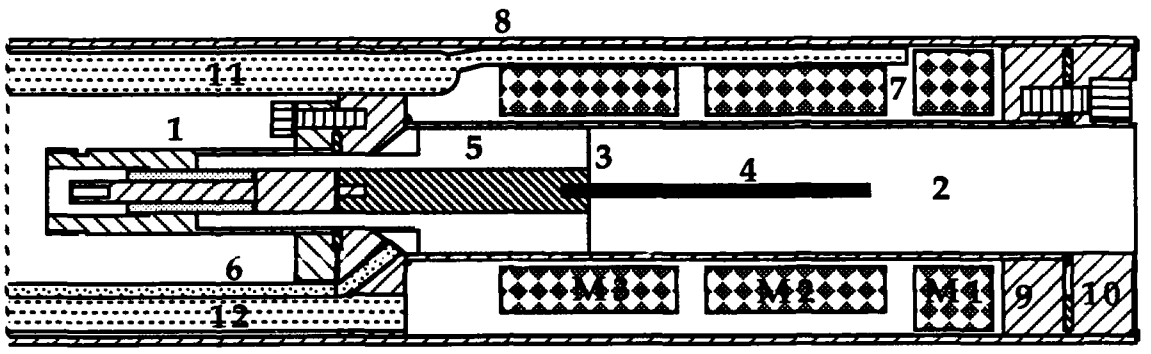

Figure A-1. Cross-sectional view of the small ECR plasma source. The numbered elements are: (1) N-type, 50 Ω coaxial feedthrough, (2) plasma cavity, (3) 50 Ω coaxial line, (4) microwave antenna, (5) boron nitride insulator, (6) gas input, (7) electro–magnets M1, M2, and M3, (8) stainless steel shell, (9) and (10) front Conflat flanges, (11) and (12) outlet and inlet for cooling water. Black points represent welded joints.

The microwave antenna was adjusted in length and diameter to produce a stable and uniform discharge. The best results regarding stability and tunability of the plasma were obtained at a length between one-quarter and one-half λ of the microwaves (λ = 12.2 cm). The diameter of the antenna affected the radial profile of the plasma beam. Large diameters (>4 mm) were found to produce a 'hollow' beam, while the 'hole' was eliminated, when antennas with diameters less than 2 mm were used.

Gases are introduced into the chamber from the back side of the source (6) through a variable UHV leak valve and guided in a coaxial manner between the outer shell and the boron nitride insulator to the plasma cavity. The plasma cavity is surrounded by three water cooled electromagnets (7) which were optimized in cross-sectional dimensions to the available space in the existing MBE system. The entire source is placed in a 13" long, 2.25" diameter stainless steel tube (8), welded on a standard 4.5" Conflat® flange. The UHV seal between the tube and the source is provided by two specially designed Conflat flanges (9,10), which accept standard copper gaskets, but have bolt holes on the inner side.

Magnets. The magnets were designed to meet several requirements: 1) axial magnetic field densities in the excess off 875 G which is required for electron cyclotron resonance at 2.45 GHz, 2) an effective mirror magnetic field which provides higher plasma densities in the cavity, 3) an effective extraction magnetic field for the formation of a plasma beam and finally 4) the dissipation of minimum energy which minimizes both the cooling requirements and the space needed for the cooling lines.

All magnets were wound on thin stainless steel spools. The two rear magnet coils (M2 and M3) have 380 turns of 0.8 mm thick copper magnet wire. Each coil produces a peak axial magnetic field density of 105 G for each Ampere of current. The front magnet has been designed to provide maximum ion extraction and has 150 turns of the same wire. The rear magnet (M3), which produces the resonant magnetic field is normally operated at 10 A, while the mirror and the extraction magnets run at 8.5 A. Filtered tap water with a flow rate of 1–1.5 l/min is used to cool the magnets. The position of the magnets along the source axis can be controlled during operation by using the push rods attached to the magnet spools. Position and separate current controls for each magnet provided excellent flexibility for preliminary testing and optimization of the source operation. The magnetic field density distribution along the source axis is shown in Figure A-2(a).

As a first approximation, ions leaving the plasma cavity follow magnetic flux lines, which diverge from the center of the front magnet. As such, one should guide as many magnetic lines as possible beyond the front edge of the source shell. These lines should not be allowed to terminate on the inner walls of the plasma cavity. This would be less problematical, if the two massive front UHV flanges (parts 9 and 10 of Fig. A-1), which extend the source ≈25 mm beyond the edge of the front magnet (M1), were replaced with a permanent, welded seal between the ECR head and stainless steel shell. However, by making this change the source would lose the flexibility which is

desired for initial testing and adjustments. The flow of the magnetic flux lines inside the source can be seen in the Figure A-2(b).

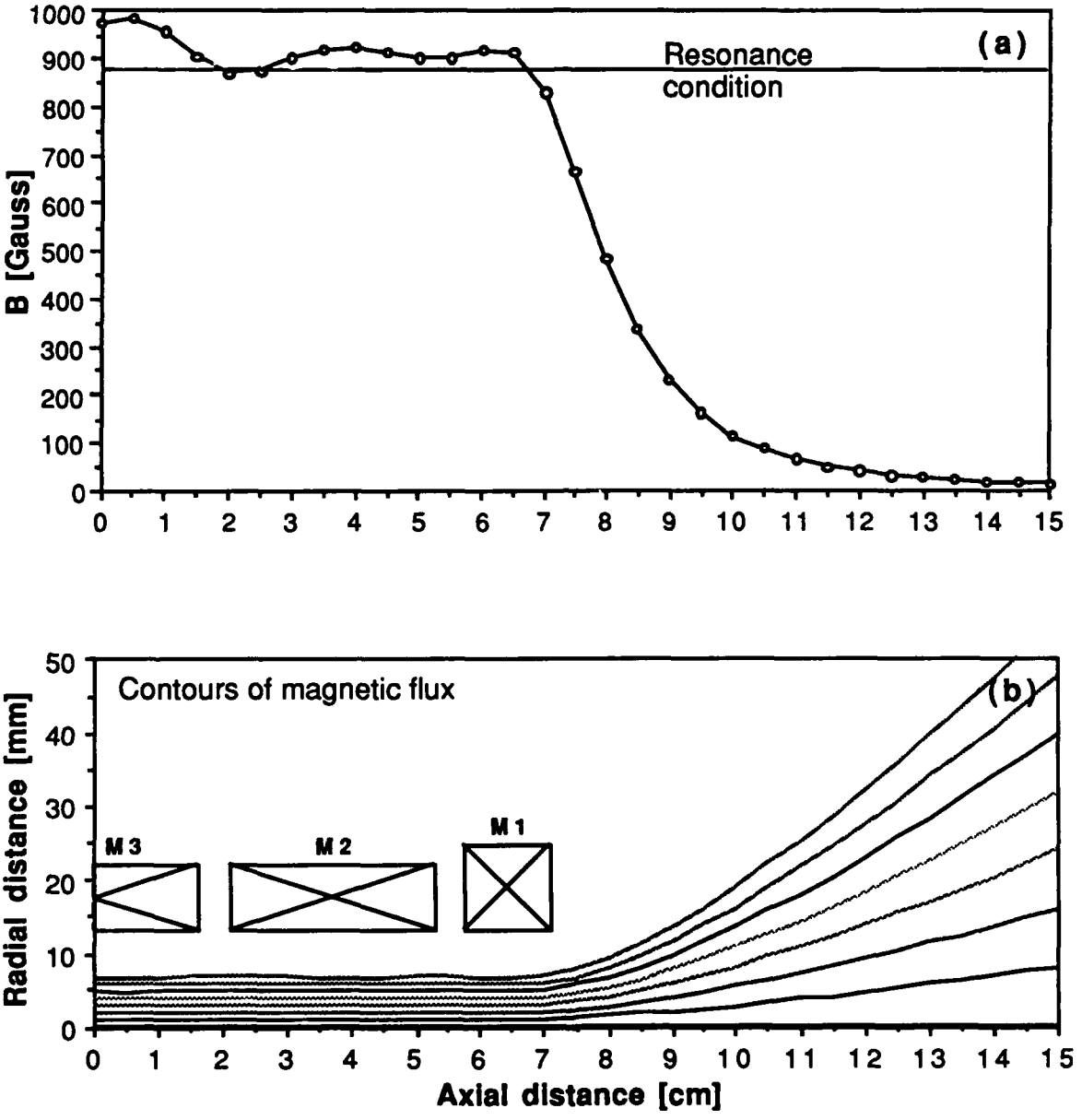

Figure A-2. (a) Distribution of the magnetic field density as measured along the source axis. Solid line indicates the value required for the ECR at 2.45 GHz. (b) The flow of magnetic flux lines produced by the above magnetic field.

Microwave system. A schematic diagram of the microwave system is shown in Figure A-3. It consists of a continuously variable, 120 W, 2.45 GHz microwave power supply (Opthos§) having a bidirectional coupler located at the output of the oscillator. Two power meters measure total forward and reflected microwave power with the difference being equal to the power coupled into the plasma cavity. The microwaves are transmitted through a 50 Ω coaxial line with a sliding slug tuner, which is capable of matching impedance differences to a ratio of 1:10. This

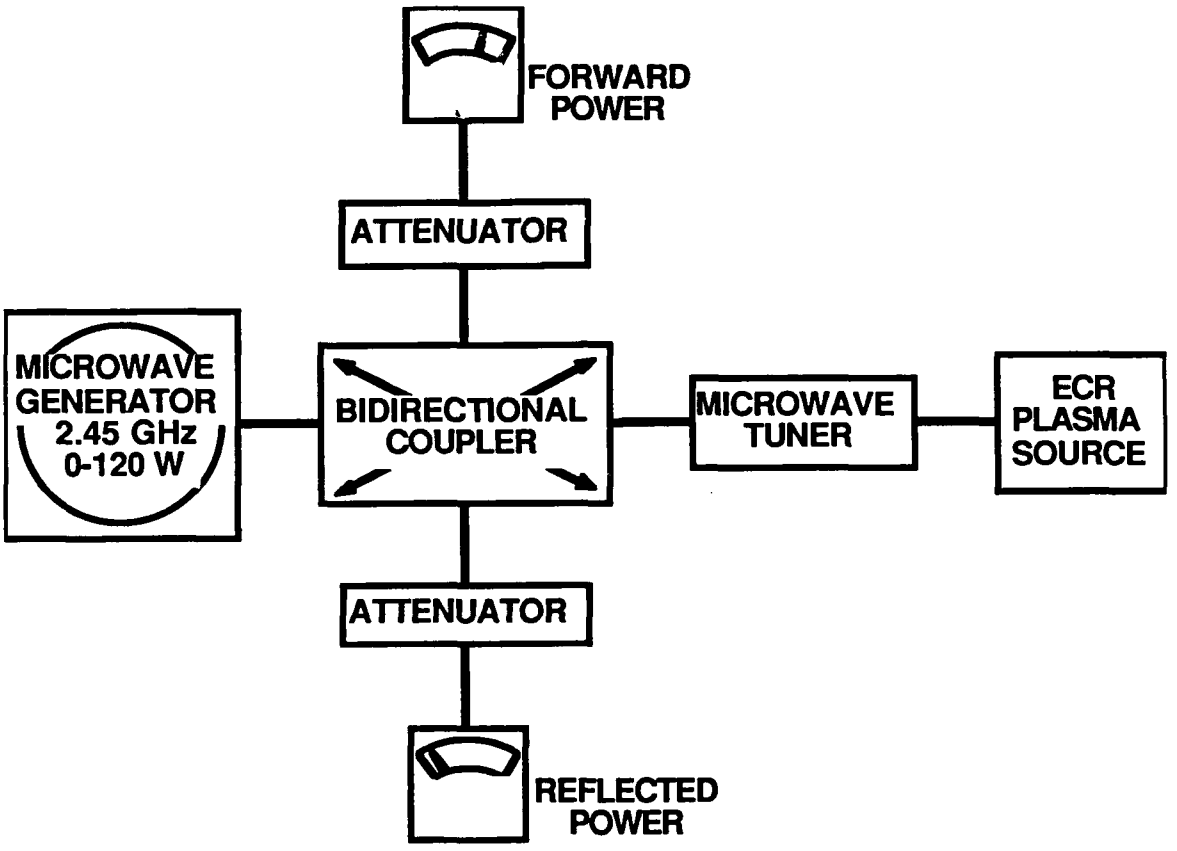

Figure A-3. Schematic diagram of the complete microwave system.

simple system and matched source head enable us to maintain the reflected power at ≈0 W, when properly tuned. Only minor additional tuning is needed following changes in power level or gas pressure. Because of this and the excellent stability over hours

§ Opthos Instruments, Inc.,17805 Caddy Dr., Rockville, MD 20855

of operation, no circulators or matched dummy loads are used to protect power generator damage which could occur under extended operation at high reflected power levels.

No initiation of ionization is needed, since breakdown starts at $\approx 1 \times 10^{-4}$ Torr and at an input power less than 10 W. A stable discharge can be maintained over four decades of pressure ranging from 10^{-5} to 10^{-1} Torr.

A-III. Plasma Characteristics

Plasma beam parameters were measured using a single cylindrical Langmuir probe (ASTeX[#]) having an area of 0.1 cm^2, a single grid Faraday cup with the collecting plate area of 1 cm^2, and a quadrupole mass spectrometer.

The source was initially characterized in a small vacuum chamber (a six-way cross with 8" ports) evacuated by a 400 l/s turbo-molecular pump. The amount of gas introduced in the source was controlled by an UHV leak valve and monitored by an ionization gauge placed in the vacuum chamber.

Ions are extracted from the source by the magnetic field gradient generated by the divergent magnetic field of the existing source magnets. Electrons are accelerated by the interaction between their magnetic moments and the magnetic field gradient. Since electron mobility is much higher than ion mobility, electrons stream out along the magnetic flux lines much faster than ions. In order to achieve neutralization between electron and ion fluxes, a static electric field is generated in the plasma stream, which accelerates positive ions in the direction of the diffusion of electrons. Because of the neutralization requirement, electrons and ions can not act independently in the ECR plasma stream, thus they must move with the same diffusion coefficients.

The plasma floating potential, V_f, has been measured outside the plasma source along the beam axis. Values of V_f were determined at several points along the plasma stream from the Langmuir probe characteristics as the required applied

[#] Applied Science and Technology, 35 Cabot Rd., Woburn, MA 01801

potential for zero probe current. For a nitrogen plasma at 50 W of microwave power and at $1x10^{-4}$ Torr (which corresponds to a gas flow rate of ≈3 sccm), the value of V_f decreased parabolically with downstream distance from the source, as shown in Figure A-4. The value of V_f is also dependent on the pressure, power and especially on the magnetic field gradient[A-9].

The ion current density, J_i, was also measured along the plasma stream by using a Langmuir probe and an in-house constructed single grid Faraday cup with collecting plate area of 1 cm^2. In order to maintain the same probe–to–plasma potential difference in all positions of the probes along the stream, a negative bias, 50 V lower than V_f at the corresponding distance from the source, was applied to the Langmuir probe or to the collecting plate of the Faraday cup. Discrepancies in the measured ion current densities obtained by both probes were less than 10%. As expected, the ion

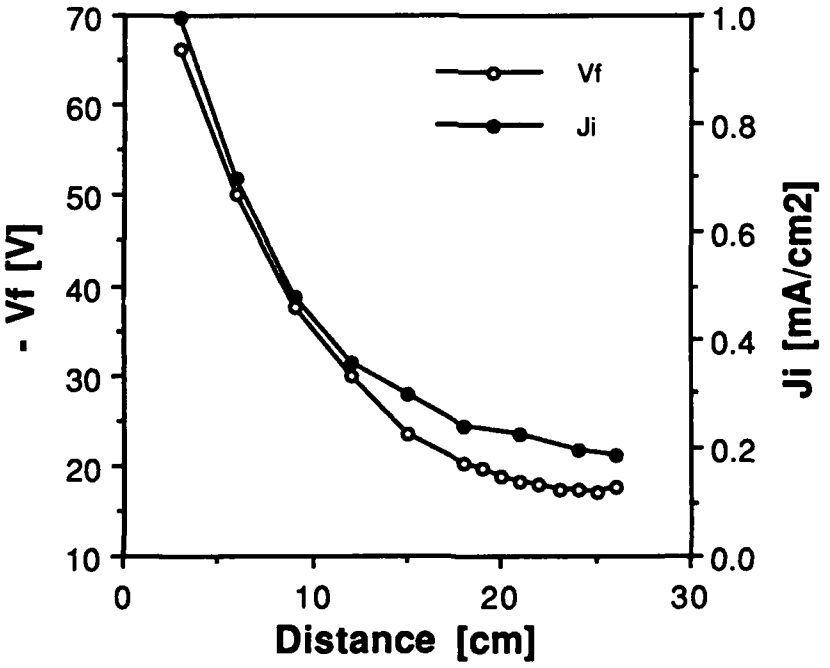

Figure A-4. The floating potential (V_f) and ion current density (J_i) vs. distance along the beam axis from the plasma source. Data are for a nitrogen plasma at 50 W of absorbed microwave power and a pressure of $1x10^{-4}$ Torr.

current density also decreased parabolically with downstream distance from the source, as shown in Figure A-4. The value of J_i also depends on the gas pressure and the excitation power. Diagrams of ion current density as a function of (1) nitrogen pressure from $1x10^{-4}$ to $8x10^{-4}$ Torr at a constant excitation power of 50 W, (2) power level from 10 to 120 W at a constant pressure of $1x10^{-4}$ Torr are shown in Figures A-5 and A-6, respectively.

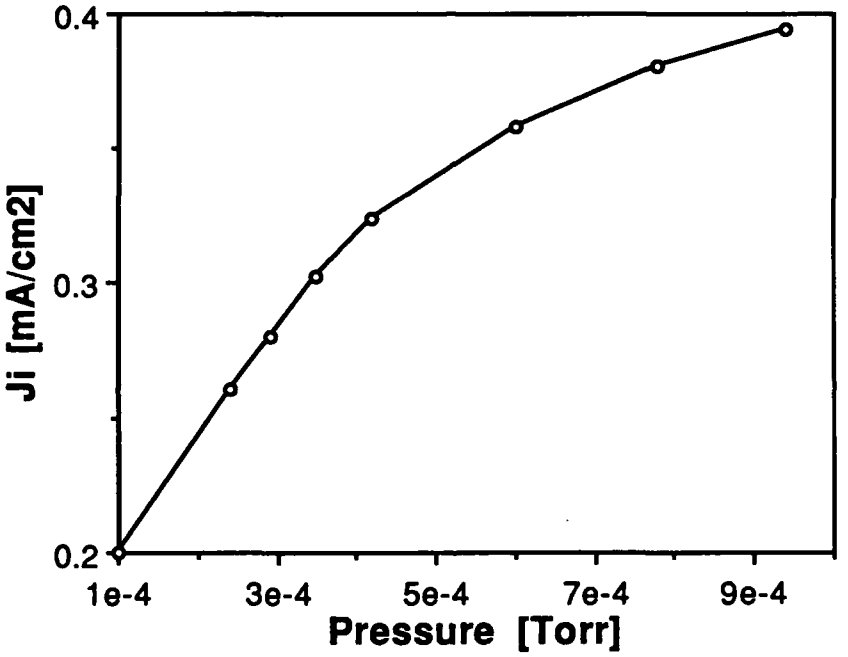

Figure A-5. Nitrogen ion current density vs. pressure. Probe was 25 cm from the source and the absorbed microwave power was 50 W.

Ion current density vs. voltage measurements were also taken at several positions along the plasma stream in order to measure electron temperature and ion density. The electron temperature, T_e, was calculated as the slope of the $\ln(J_i)$ vs. V curve for applied potentials greater than the floating potential. Ion density, n_i, was then calculated from known values of T_e and J_i as:

$$n_i = \frac{J_i}{ce_o\sqrt{\frac{2kT_e}{m_i}}},$$

where c is a geometrical probe factor (0.4 for cylindrical probes), e_o is electron charge, k is Boltzman's constant and m_i is the average mass of the ions. The sheath around the probe was not taken into account, since it is expected to be thin for low pressure plasmas, where the mean free path and Debye length are much larger than the probe dimensions [A-10].

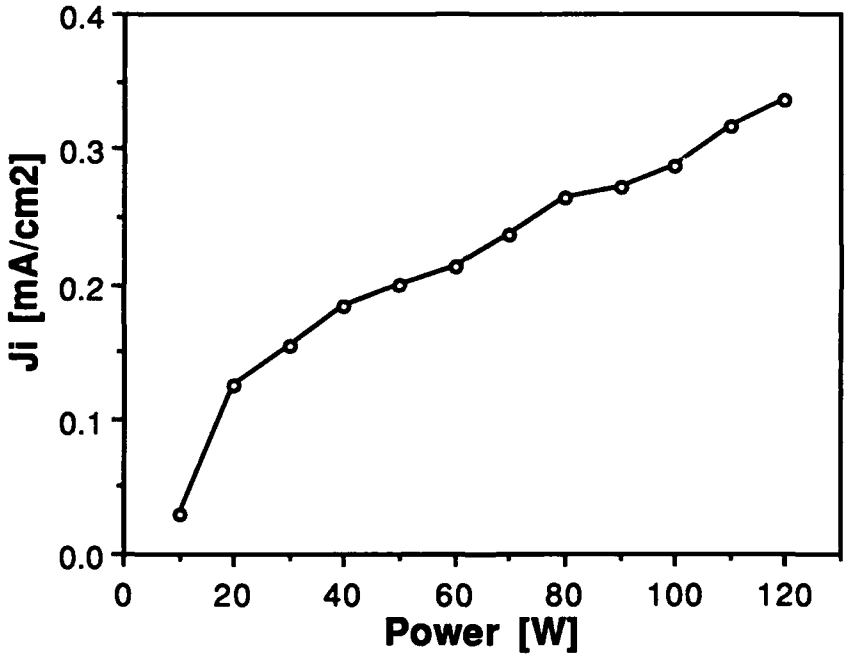

Figure A6. Nitrogen ion current density vs absorbed microwave power. Total gas pressure was constant at $1x10^{-4}$ Torr.

Values of ion densities and electron temperatures from different points along the plasma stream are shown in Figure A-7. Electron temperatures above 100,000 K and ion densities $\approx 1x10^{10}$ were measured for the nitrogen plasma stream outside the plasma cavity, again at an absorbed microwave power of only 50 W and pressure of $1x10^{-4}$ Torr. Using plasma brightness as an indicator, the ion densities near the

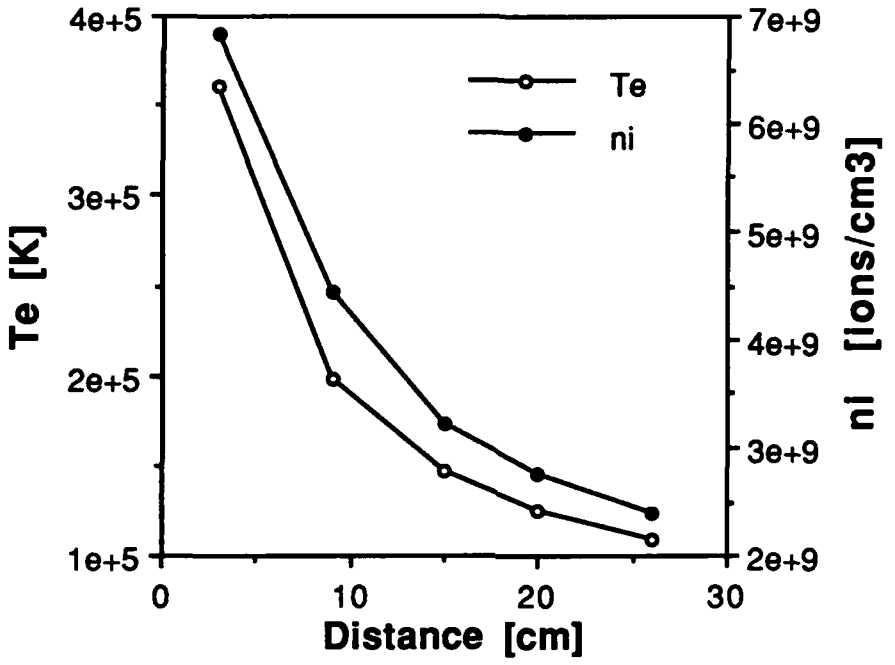

Figure A-7. *Electron temperature (T_e) and ion density (n_i) in the plasma beam as a function of distance from the source. Data are for a nitrogen plasma at 50 W of absorbed microwave power and a pressure of $1x10^{-4}$ Torr.*

resonance region inside the source were estimated to be at least one or two orders of magnitude higher than those measured along the plasma beam.

As already mentioned, the radial profile of the plasma beam depends upon the diameter of the microwave antenna. The beam was found to be 'hollow', i. e., to posses lower ion current densities in the center than on the edges for antennas with diameters larger than 5 mm. However the profile changed for diameters smaller than 2 mm. Radial profiles of the plasma beams, obtained when 5 mm and 1 mm microwave antennas were applied, are shown in Figure A-8. The ion current density increased to a certain distance from the center of the beam for the 5 mm antenna, while it monotonically decreased for the 1 mm antenna. Measurements were taken 20 cm from the source using the same values of the other parameters as in the J_i- V measurements.

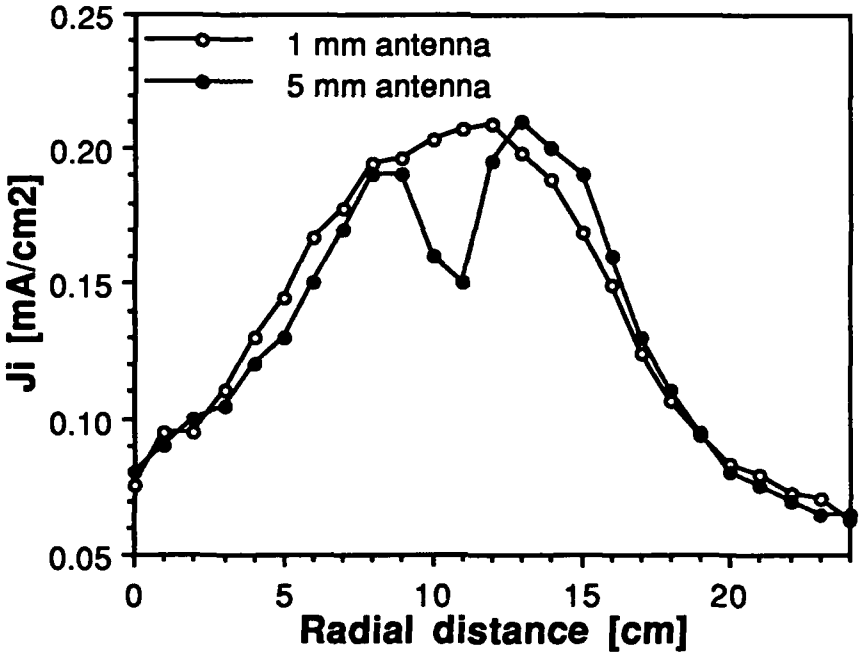

Figure A-8. Radial profiles of the nitrogen plasma beam in terms of ion current density for the microwave antenna diameters of 1 and 5 mm. Probe was 20 cm from the source. An absorbed microwave power of 50 W and a pressure of $1x10^{-4}$ Torr were used in this experiment.

The source performance was also examined with a hydrogen plasma. Ion current densities for this plasma were 5-6 times higher than the ones measured for the nitrogen plasma at the same excitation power and gas flow rates. No additional tuning was required for the transition from one gas to the other. Thus substrates may be cleaned in-situ with hydrogen followed immediately by the deposition of the nitrides.

Langmuir probe current vs. voltage characteristics measured for both gases at 15 cm from the source and at absorbed microwave power of 50 W are shown in Figure A-9. In addition to the aforementioned higher J_i for the hydrogen plasma two other differences can be observed from these two characteristics. Firstly, the electron temperature in the hydrogen plasma (70,000 K) is much lower than in the nitrogen plasma (120,000 K). Secondly, the value of V_f, at this distance, for the hydrogen plasma is positive (5 V) and for the nitrogen plasma negative (–15 V).

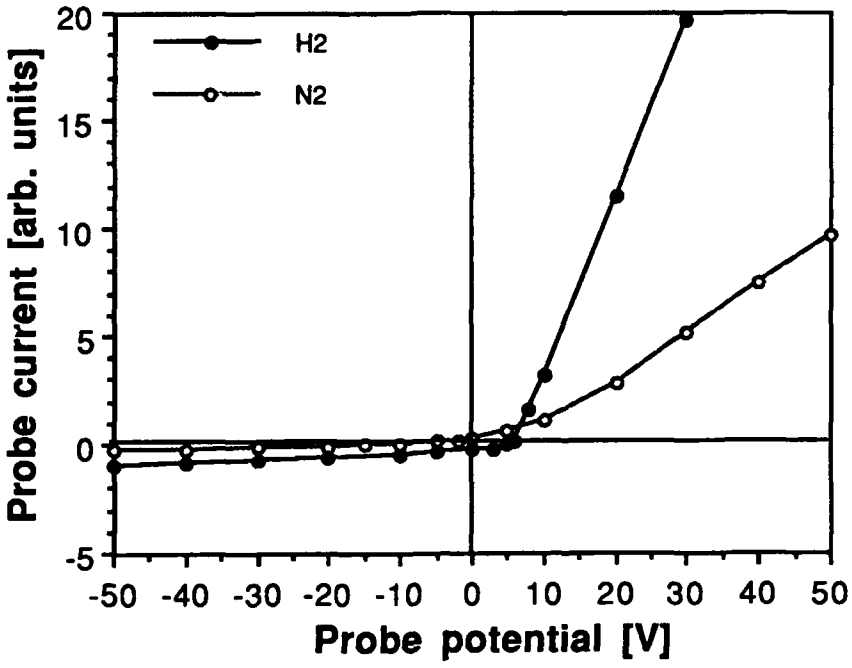

Figure A-9. I–V Langmuir probe characteristics measured at 15 cm from the source for nitrogen and hydrogen plasma beams. All measurements were taken at 50 W and a gas flow rate of 3 sccm.

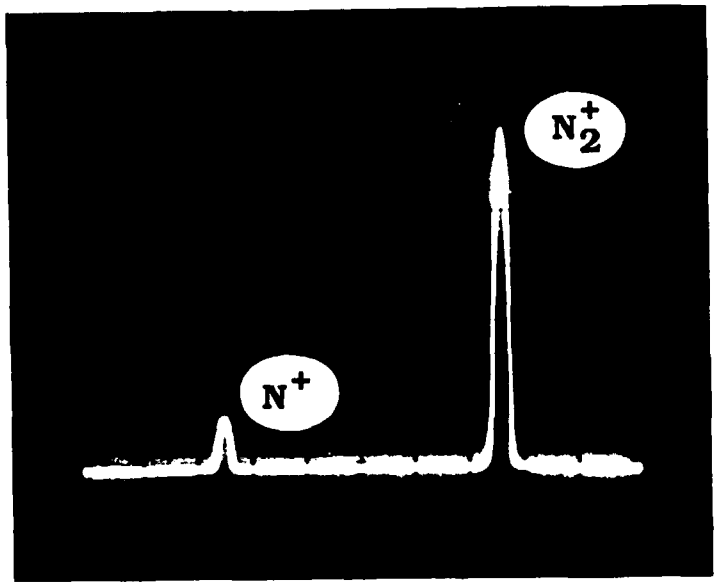

Figure A-10. Output of a quadrupole mas spectrometer showing N^+ and N_2^+ peaks. The N^+/N_2^+ ratio is 0.15–0.2.

The ion species in the extracted beam were analyzed with a quadrupole mass spectrometer. Results obtained for a nitrogen plasma excited at 50 W and a pressure of $1x10^{-4}$ Torr are shown in Figure A-10. The percentage of N^+ in the beam was 15-20%; this ratio changed only slightly with pressure or microwave power.

A-IV. Growth Results

A. Gallium Nitride Layers

Overview. The GaN films were deposited using the following substrates and temperature ranges: (0001) sapphire (500-800°C), (0001) and (000$\bar{1}$) α(6H)–SiC (500-800°C), (100) β–SiC (550-650°C), (0001) ZnO (600-700°C), (001) TiO_2 (550-700°C), and (100) Si (550-700°C). The lattice mismatches between these substrates and GaN are given Table A-I. The predeposition treatment of the substrates has been described previously[A-11].

Transmission electron microscopy (TEM) (Hitachi H-800) and high resolution

Table A-I: The lattice mismatch between GaN and various substrates.

Substrate Material	Structure	Growth Plane	Lattice Parameter [nm]	$\frac{\lvert a_s - a_{GaN} \rvert}{a_s}$
Sapphire	Rhombohedral	(0001)	0.476^H	0.336^H
α(6H)–SiC	Wurtzite	(0001)	0.308	0.026^H
ZnO	Wurtzite	(0001)	0.325	0.028^H
TiO_2	Tetragonal	(001)	0.459	0.017^C
β–SiC	Zinc Blende	(100)	0.436	0.034^C
Si	Diamond	(100)	0.543	0.169^C
wGaN	Wurtzite	(0001)	0.316	1.000^H
cGaN	Zinc Blende	(100)	0.451	1.000^C

^{H}hexagonal structure, ^{C}cubic structure

microscopy (HREM) (JEOL 200CX) were used to analyze the grown films. Cross-sectional TEM specimens were prepared using standard techniques[A-12]. Imaging at different g vectors and dark field imaging were used to bring into contrast a particular type of defect.

Structural Analysis. GaN films grown on α–SiC, β–SiC, and ZnO were monocrystalline under all deposition conditions. Films grown on sapphire were monocrystalline when grown at a temperature higher than 600°C but showed a columnar structure with low angle (<10°) grain boundaries when grown at a lower temperature, as determined from HREM and electron diffraction studies. GaN grown on (100) Si was oriented-polycrystalline with the c–axis of GaN perpendicular to the growth direction, while GaN on TiO_2 (despite apparently good lattice match) grew polycrystalline without a preferential orientation, as determined by reflection high energy electron diffraction (RHEED) and x–ray diffraction.

Figure A-11 shows TEM images of the wurtzite GaN films deposited on the basal planes of sapphire, α–SiC C-face, and ZnO, taken at two perpendicular g vectors. Two different types of defects with very high density can be seen, one parallel to the (0001) planes (Figure A-11 (a1-a3)) and the other perpendicular to them (Figure A-11 (b1-b3)).

The defects parallel to the (0001) planes were in contrast when g=$(10\bar{1}0)$ (stronger) and g=$(2\bar{1}\bar{1}0)$ (weaker) and invisible at g=(0002). Thus they have the displacement vector perpendicular to the [0001] direction. These defects are very likely to be rotational domains, rotated relative to each other around the [0001] direction by 60°. This rotation is equivalent to the displacement of $1/3[10\bar{1}0]$. Rotational domains have been observed in other materials[A-13–A-14] but have not been previously identified in GaN. The probability of finding such domains is high for both close packed structures, hexagonal and cubic, since they both offer two equivalent types of tetrahedral sites on (0001) and (111) planes, respectively. The

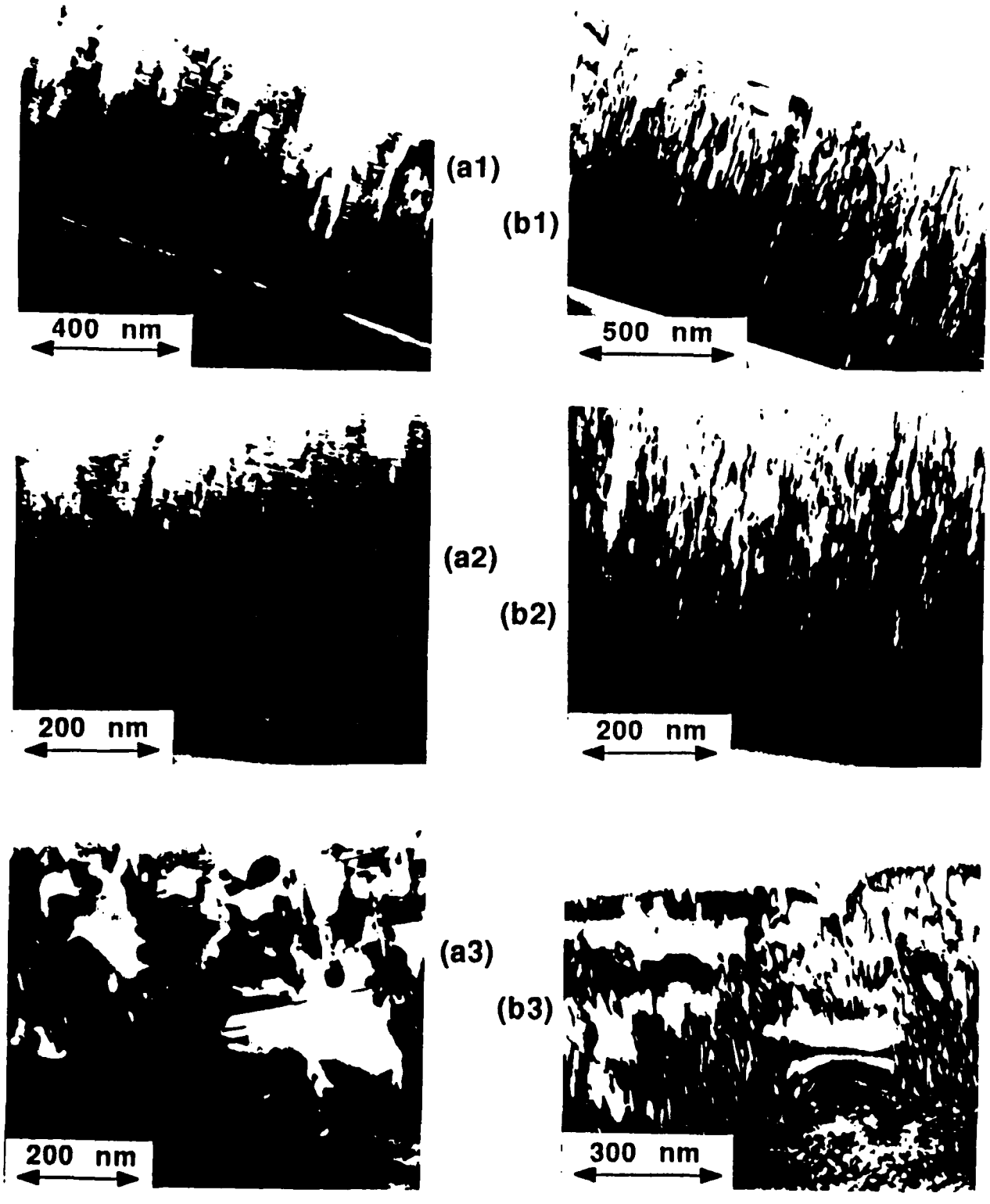

Figure A-11. TEM images of wurtzite GaN grown at 650°C on the basal planes of sapphire (1), α(6H)–SiC C-face (2), and ZnO (3) taken at g=(10$\bar{1}$0) (a1–a3) and g=(0002) (b1–b2).

boundary formed where rotated nuclei grow together is termed a double positioning boundary (DPB) or rotational twin boundary. The formation of a DPB is illustrated in Figure A-12. A rotational domain can easily disappear and reappear during the growth, since every third plane of Ga–N pairs has the potential to form a perfect bond across the interface between two rotated domains, or to start growth in a rotated position on a previously perfect plane. Across a DPB can be found either pairs of two occupied or two empty tetrahedral sites, while away from it exist only occupied–empty pairs (see Figure A-12). As such, DPBs may have numerous vacancies associated with them. Since these defects are very dense they may contribute considerably to the electronic properties of GaN. However, more work is needed to precisely identify the electronic nature and behavior of these defects.

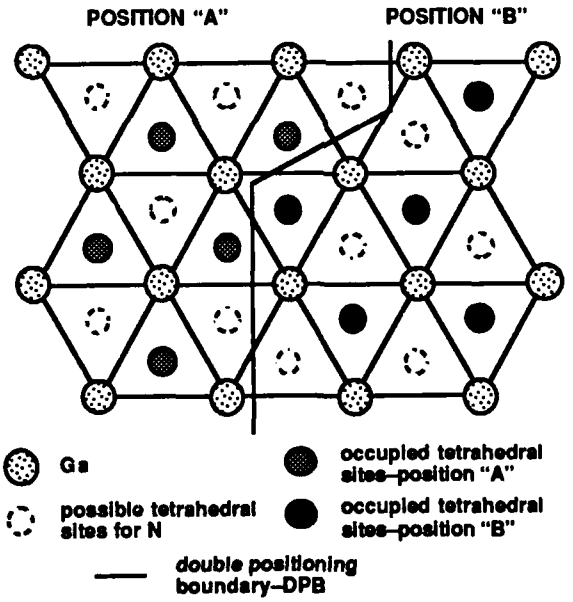

Figure A-12. An illustration of the formation of DPB when two domains rotated for 60° grow together. Note the difference in the occupation of the tetrahedral sites at the boundary and away from it.

The defects perpendicular to the (0001) planes and in contrast for g=(0002), are misfit dislocations and IDBs (Figure A-11(b1–b3)) but because of their high density and also high strain contrast, they were difficult to resolve. The presence of

IDBs was confirmed by HREM (Figure A-13(a)), where the fractional misalignment of the lattice fringes of (0002) planes can be seen.

A rotational domain can easily disappear and reappear during the growth, since every third plane of Ga–N pairs has the potential to form a perfect bond across the interface between two rotated domains, or to start growth in a rotated position on a previously perfect plane. Across a DPB can be found either pairs of two occupied or two empty tetrahedral sites, while away from it exist only occupied–empty pairs (see Figure A-12). As such, DPBs may have numerous vacancies associated with them. Since these defects are very dense they may contribute considerably to the electronic properties of GaN. However, more work is needed to precisely identify the electronic nature and behavior of these defects.

The defects perpendicular to the (0001) planes and in contrast for g=(0002), are misfit dislocations and IDBs (Figure A-11(b1–b3)) but because of their high density and also high strain contrast, they were difficult to resolve. The presence of IDBs was confirmed by HREM (Figure A-13(a)), where the fractional misalignment of the lattice fringes of (0002) planes can be seen.

The density of all these defects slowly decreases with distance from the GaN/substrate interface. The changes of the growth temperature in the range of 500-800°C did not seem to change their density dramatically. The highest quality GaN appears to grow on ZnO, however more research is needed to make this a concluding statement. The films grown on (0001) α-SiC showed a lower defect density than the ones grown on $(000\bar{1})$. This may be due to the surface graphitization of α-SiC discussed by Bommel *et al* [A-15]. Improved surface and optical character of GaN grown on the (0001) surface of α-SiC has been reported also by Saski and Matsuoka [A-16].

Figure A-13. (a) HREM image of the wurtzite GaN grown on the basal plane of sapphire at 650°C (arrows denote IDBs). (b) HREM image of the zinc–blende GaN grown at 600°C on (100) plane of β-SiC showing microtwins and stacking faults emanating from the heteroepitaxial interface.

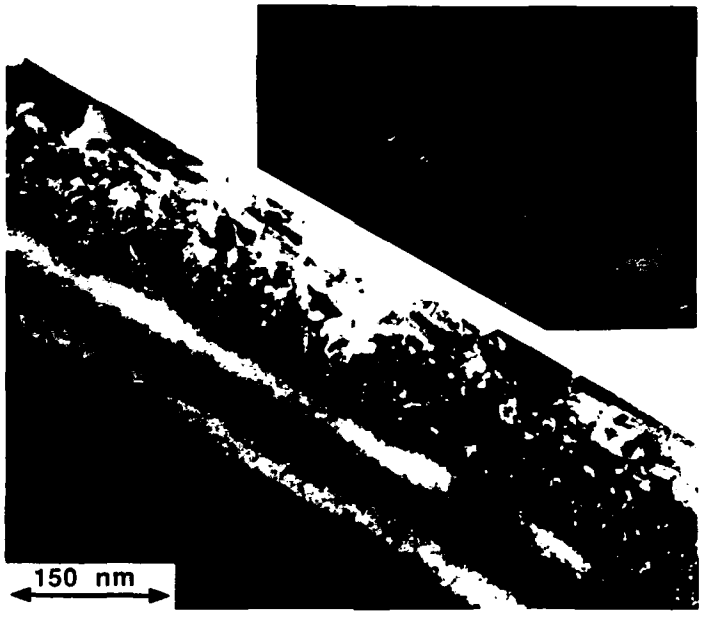

Figure A-14. Complementary bright and dark field images of zinc–blende GaN grown on β–SiC. A 111-type twin reflection was used to obtain the dark field image.

The microstructure of zinc-blende GaN grown on (100) β–SiC was quite different Figure A-14. The defects consisted of threading dislocations and planar

defects parallel to the (111) planes. The defect density in these films decreased with the distance from the GaN/SiC heteroepitaxial interface. Complementary bright field (Figure A-14(a)) and dark field (Figure A-14(b)) micrographs were taken from the cross-sectional samples. The dark field image was obtained by using a 111-type twin reflection, and hence, many of the planar defects were found to be microtwins. The majority of microtwins emanate from the heteroepitaxial interface but do not extend to the free surface of the film. Most microtwins have been found to terminate within a distance of 25 nm. This type of microtwin morphology has also been observed in several other heteroepitaxial systems[A-17–A-18].

B. Mg-Doping of GaN

Amano *et al*, [A-19] recently reported the ability to produce *p*-type GaN layers by electron beam irradiation of Mg-doped GaN. The electron beam irradiation was apparently essential to the formation of the *p*-type layer. Therefore a supply of magnesium was purchased and installed in the effusion cell reserved for dopants. A SIMS reference standard for the determination of the Mg doping level was produced. This standard is also being used for the calibration of the Mg cell.

At present, our samples are electron beam irradiated after growth using an SEM. The resistivity of the doped samples increased significantly (a few orders of magnitude) after electron beam irradiation. Samples having the proper Mg concentration became p-type, as confirmed by the I–V measurements conducted using a Mercury probe and by thermal probing. Figure A-16 shows a set of I–V curves obtained from a Mg–doped sample after different irradiation times. Note the increase in the resistivity and the curve asymmetry. C–V measurements on one sample showed a p–type carrier concentration in the range of 10^{18} cm^{-3} which is much higher than reported by Amano *at al.* Preparations for high and low temperature Hall measurements are being conducted, which should unambiguously confirm the nature of

the conductivity as well as give the associated activation energies carrier concentrations and mobilities.

A photo–assisted MBE process has also been considered for the activation of dopants. A photo–irradiation system has been designed

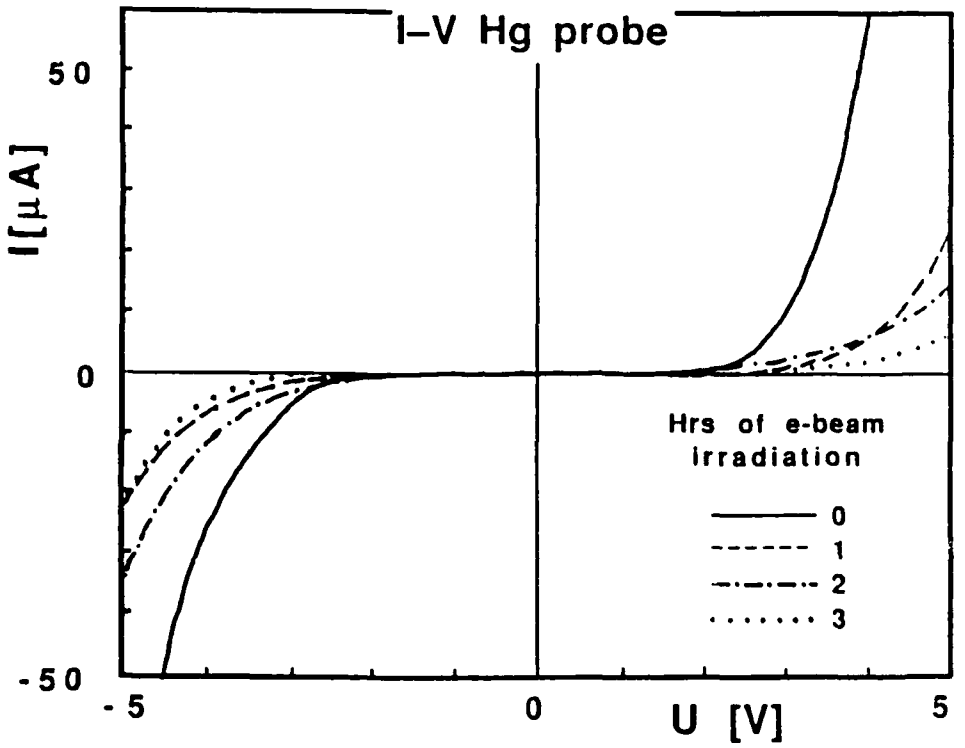

Figure A-16. I–V curves of Mg doped and electron beam irradiated GaN. The parameter is irradiation time and is currently being constructed. In contrast to the electron irradiation, photo irradiation will be applied *in situ* during the growth process.

A-V. References

A-1. J. Sakamoto, Jpn. J. Appl. Phys. 16, 1993 (1977).

A-2. R. R. Burke and C. Pomot, Solid State Technol.31, 67 (1988).

A-3. L. Mahoney, M. Dahimene, and J. Asmussen, Rev. Sci. Instrum. 59, 448 (1988).

A-4. T. Ono, C. Takahashi, and S. Matsuo, Jpn. J. Appl Phys. 23, L534 (1984).

A-5. A. Chayara, A. Masuda, T. Imura, and Y. Osaka, Jpn. J. Appl. Phys. 25, L564 (1986).

A-6. S. Matsuo and M. Kiuchi, Jpn. J. Appl Phys. 22, L210 (1983).

A-7. T. Ono, M. Oda, C. Takahashi, and S. Matsuo, J. Vac. Sci. Technol. B4, 696 (1986).

A-8. S. Matsuo and Y. Adachi, Jpn. J. Appl Phys. 21, L4 (1982).

A-9. M. Matsuoka and K. Ono, J. Vac. Sci. Technoll. A 4, 25 (1988).

A-10. J. D. Swift and M. J. R. Schwar, Electrical Probes for Plasma Diagnostics, American Elsevier Publishing Co., New York, 1969.

A-11. Z. Sitar, M. J. Paisley, B. Yan, J. Ruan, J. W. Choyke, and R. F. Davis, to be published in J. Vac. Sci. Technol B, March/April (1990).

A-12. J. C. Bravman and R. Sinclair, J. Electron Microsc. Technol. 1, 53 (1987).

A-13. M. J. Stowell, in Epitaxial Growth, part B, edited by J. W. Matthews (Academic Press, Inc., New York, 1975) p. 465.

A-14. H. S. Kong, B. L. Jiang, J. T. Glass, G. A. Rozgonyi, and K. L. More, J. Appl. Phys. 63, 2645 (1988).

A-15. A. J. Bommel, J. E. Crombeen, and A. van Tooren, Surface Sci 48, 463 (1975).

A-16. T. Sasaki and T. Matsuoka, J. Appl. Phys. 64, 4531 (9188)

A-17. M.E. Twigg and E.D. Richmond, J. Appl. Phys. 64, 3037 (1988).

A-18. J. B. Posthill, J. C. L. Tarn, T. P. Humphreys, K. Das, J. J. Wortman, and N. R. Parikh, Proc. 46th Ann. Meet. Electron Microsc. Soc. Am., edeted by G. W. Bailey, 896 (1988).

A-19. H. Amano, M. Kito, K. Hiramatsu, and I. Akasaki, Jap. J. Appl. Phys. 28, L2112 (1989)